JACS
JOURNAL OF THE AMERICAN CHEMICAL SOCIETY

ARTICLE

pubs.acs.org/JACS

Triazole Bridges as Versatile Linkers in Electron Donor−Acceptor Conjugates

Gustavo de Miguel,[‡] Mateusz Wielopolski,[‡] David I. Schuster,*[,†] Michael A. Fazio,[†] Olivia P. Lee,[†] Christopher K. Haley,[†] Angy L. Ortiz,[∥] Luis Echegoyen,[⊥] Timothy Clark,[§] and Dirk M. Guldi*[,‡]

[†]Department of Chemistry, New York University, New York, New York 10003, United States

[‡]Department of Chemistry and Pharmacy & Interdisciplinary Center for Molecular Materials, Friedrich-Alexander-Universität Erlangen-Nürnberg, 91058 Erlangen, Germany

[§]Computer-Chemie-Centrum, University of Erlangen, 91052 Erlangen, Germany

[∥]Department of Chemistry, Clemson University, Clemson, South Carolina 29634, United States

[⊥]Department of Chemistry, University of Texas at El Paso, El Paso, Texas 79968-0519, United States

Supporting Information

ABSTRACT: Aromatic triazoles have been frequently used as π-conjugated linkers in intramolecular electron transfer processes. To gain a deeper understanding of the electron-mediating function of triazoles, we have synthesized a family of new triazole-based electron donor−acceptor conjugates. We have connected zinc(II)porphyrins and fullerenes through a central triazole moiety—(ZnP−Tri−C_{60})—each with a single change in their connection through the linker. An extensive photophysical and computational investigation reveals that the electron transfer dynamics—charge separation and charge recombination—in the different ZnP−Tri−C_{60} conjugates reflect a significant influence of the connectivity at the triazole linker. Except for the *m*4*m*-ZnP−Tri−C_{60} **17**, the conjugates exhibit through-bond photoinduced electron transfer with varying rate constants. Since the through-bond distance is nearly the same for all the synthesized ZnP−Tri−C_{60} conjugates, the variation in charge separation and charge recombination dynamics is mainly associated with the electronic properties of the conjugates, including orbital energies, electron affinity, and the energies of the excited states. The changes of the electronic couplings are, in turn, a consequence of the different connectivity patterns at the triazole moieties.

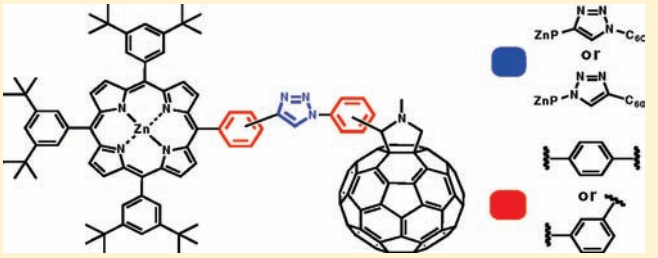

INTRODUCTION

Natural photosynthesis has evolved to separate charges efficiently and use the potential of this charge imbalance to drive reactions.[1,2] Artificial photosynthetic mimics can imitate a charge imbalance by manipulating the rates of charge separation (CS) and charge recombination (CR).[3−6] If the rate of intramolecular CS (k_{CS}) is greater than the rate of intramolecular CR (k_{CR}), a long-lived charge-separated state can be achieved. The Marcus theory of electron transfer describes the parameters governing electron transfer (ET) rates and provides the theoretical framework for designing donor−acceptor systems capable of achieving long-lived charge-separated states.[7]

Due to the complexity of the components of the ET chain in natural photosynthesis, researchers have drastically simplified the process using model systems. These artificial systems incorporate an electron donor, an electron acceptor, and a bridging unit.[3] The donor in many of these systems is a porphyrin or phthalocyanine due to the relative ease of synthesis, stability, low ionization potential, and excellent light absorption properties of these materials.[8] The electron acceptor in many model systems is [60]-fullerene (C_{60}) which has superior acceptor properties, most importantly low reduction potential and low reorganization energy.[9] The third important unit in these systems is the bridging unit, which provides the most significant differences between various artificial photosynthetic mimics.[10] While the major emphasis of research in this area has involved covalently linked donor-C_{60} systems,[11] attention has been focused recently on mechanically interlocked supramolecular donor-C_{60} systems.[12]

While the donor and acceptor moieties of an artificial photosynthetic system are absolutely crucial to the function of the system, these two components alone are not sufficient to achieve a long-lived charge-separated (CS) state. Fluorescence spectroscopy shows that a mixture of donor and acceptor in solution at micromolar concentrations does not significantly lead to quenching of the donor excited state by intermolecular electronic interactions. Simply introducing a bridge between the two units, however, has a drastic effect on the electron and energy transfer rates and efficiencies of the system.[13]

Received: March 18, 2011
Published: June 27, 2011

The bridging unit in artificial photosynthetic mimics performs two functions: it acts as a conduit through which ET is facilitated, and it serves to orient the two chromophores at set distances and bond angles. These functions are seen in natural systems: the donor−acceptor cofactors are embedded in the reaction center and cell membrane at optimal distances from each other to carry an electron down a potential gradient over a distance that makes CR along the same path essentially impossible.[1] Thus, the goal of research into artificial photosynthetic systems is to transfer the electron from the donor to the acceptor at a fast rate while retarding the CR rate as much as possible, thus enhancing the lifetime of the CS state. This is an important factor in applications of organic materials in solar energy storage and photovoltaic devices.[2−6,8,10,12]

"Click chemistry" is a term widely used to define a particular class of chemical reactions that have gained much attention from the scientific community in the past decade.[14] The main attributes of these reactions are reliability (high yield of intended products), selectivity (little or no byproduct), functional group tolerance, and simplicity of reaction conditions. Among the chemical transformations that meet all of these requirements, the copper-catalyzed azide−alkyne cycloaddition (CuAAC), producing 1,2,3-triazoles, is considered to be a premier example.[12,15] As a result, the 1,2,3-triazole group has become a widely utilized chemical linker that provides a straightforward way to covalently connect precursor fragments containing azide and alkyne groups.[16] The great versatility of the "click" cycloaddition reaction has led to a wide range of applications in, for example, bioconjugation,[17] materials science,[18] and drug discovery.[19] In particular, the CuAAC has been used in the synthesis of dendronized linear polymers containing photoactive molecules[20] and in the functionalization of the surface of single-wall carbon nanotubes with polystyrene to solubilize them in a variety of organic solvents.[21] These examples represent interesting applications in molecular electronics, which justifies our interest in determining the electronic properties of the 1,2,3-triazole linker in greater detail. In addition, aromatic triazoles have recently been shown to act as conjugative π-linkers in intramolecular ET processes,[22,23] a property we exploit in the present study by exploring the use of 1,2,3-triazoles as the linkers in a new series of ZnP-C_{60} electron donor−acceptor conjugates.

A series of triazole-linked zinc(II)porphyrin−fullerene (ZnP−Tri−C_{60}) conjugates was synthesized, each with one change in mode of connection through the linker (Figure 1). We report here on the effects of the phenyl ring connectivities and triazole orientation on the rates of CS and CR processes. Differences have been observed in past work both in attachment sites on phenyl rings and in orientation of a conjugated linker.[24] By combining the structural variations of these three moieties, we hoped to be able to fine-tune rates of CS and CR processes and to extend the CS state lifetimes beyond that of fully conjugated systems.[10] Copper-catalyzed Huisgen 1,3-dipolar cycloaddition was used to selectively synthesize 1,4-disubstituted 1,2,3-triazoles, which then serve as covalent linkers between the photo- and redoxactive porphyrins and fullerenes. Molecular modeling calculations were carried out to assess whether through-space and/or though-bond electron transfer mechanisms are feasible in these systems. Finally, photophysical studies using steady-state absorption and emission techniques and femtosecond and nanosecond transient absorption spectroscopy were used to determine absolute rate constants for the intramolecular processes occurring after photoexcitation of the ZnP−Tri−C_{60} conjugates.

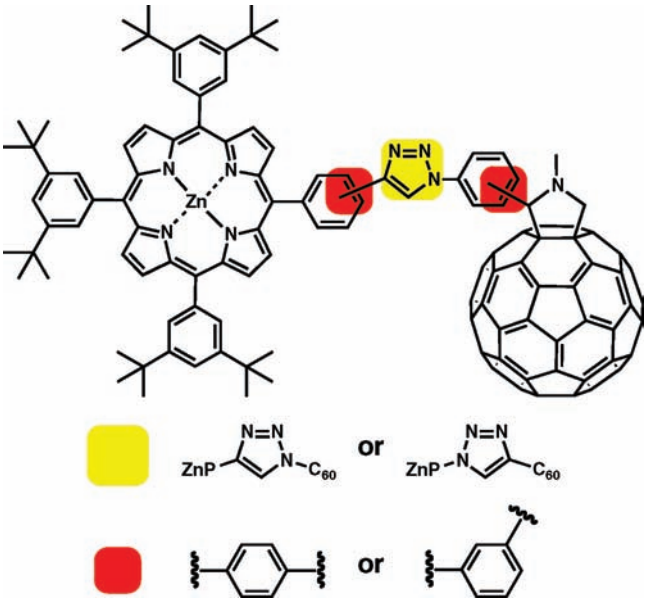

Figure 1. Structures of the triazole-linked ZnP-C_{60} conjugates highlighting the different connectivity patterns.

RESULTS AND DISCUSSION

1. Synthesis. The Huisgen 1,3-dipolar cycloaddition between an azide and a terminal alkyne results in formation of a 1,2,3-triazole ring. The uncatalyzed reaction produces both 1,4- and 1,5-disubstituted isomers, while the copper(I)-catalyzed reaction, a class of the so-called "click reactions", is regioselective for the 1,4-disubstituted isomer.[14,15] The CuAAC reaction is synthetically very useful due to its regioselectivity, the low amount of side products, high yields, short reaction times (especially in a microwave apparatus),[25] high tolerance toward functional groups on the reactants, and low toxicity of solvents used. The final step in the projected synthesis of the target zinc(II)porphyrin−triazole−fullerene (ZnP−Tri−C_{60}) conjugates involves a second 1,3-dipolar cycloaddition reaction to C_{60}, the well-known Prato reaction, via an intermediate azomethine ylide.[26]

The series of conjugates depicted in Figure 2 were synthesized incorporating a 1,4-disubstituted 1,2,3-triazole linker. In naming these compounds, the first letter designates the connection of the alkyne or azide group to the phenyl ring on the porphyrin. The number indicates whether the porphyrin is attached to the triazole ring at the 1 or 4 position. The second letter denotes the orientation of the substituents on the phenyl ring attached to the fulleropyrrolidine.

The overall synthetic scheme is depicted in Figure 3. The synthesis of the monoethynyl porphyrins was carried out by a Lindsey mixed-aldehyde condensation[27] using 3,5-di-*tert*-butylbenzaldehyde, tetraphenylphosphonium chloride, and either 3-(trimethylsilyl)ethynyl-benzaldehyde (**1**) or 4-(trimethylsilyl)-ethynyl-benzaldehyde (**2**) in dichloromethane under an argon atmosphere. Addition of pyrrole and boron trifluoride diethyl etherate afforded the porphyrinogen, which was then oxidized to the corresponding porphyrin using 2,3-dichloro-5,6-dicyano-1,4-benzoquinone (DDQ). Insertion of zinc(II) into the porphyrin using $Zn(OAc)_2$ in methanol and subsequent removal of the trimethylsilyl protecting group on the alkyne with tetrabutylammonium fluoride (TBAF) yielded alkynylporphyrins *m*-ZnP (**3**) and *p*-ZnP (**4**).

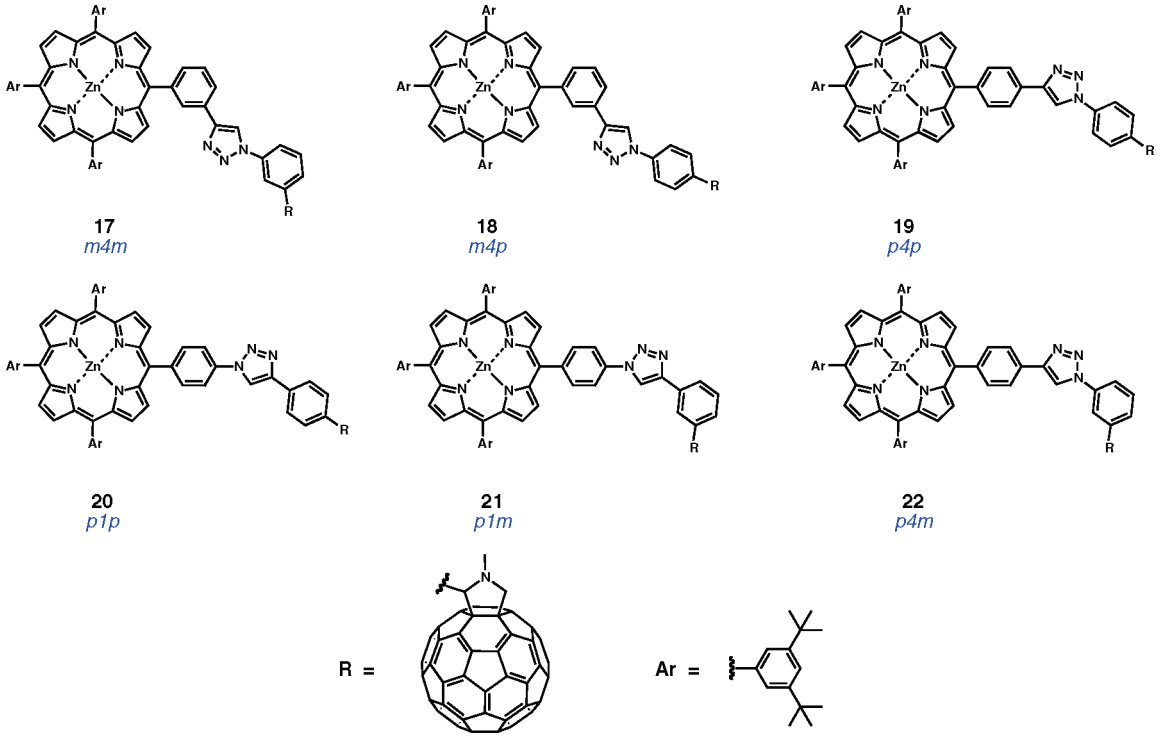

Figure 2. ZnP−Tri−C_{60} conjugates: *m*4*m* (**17**), *m*4*p* (**18**), *p*4*p* (**19**), *p*1*p* (**20**), *p*1*m* (**21**), and *p*4*m* (**22**).

This mixed-aldehyde condensation reaction afforded a number of porphyrins whose ratios are controlled by statistics, steric factors, and reaction conditions. The most prevalent porphyrins formed from this reaction are A_4, A_3B, and A_2B_2, where A and B represent the two starting aldehydes. Due to difficulties in isolating the desired A_3B porphyrins on the scale required for subsequent reactions, the unreactive nature of the tetraphenyl A_4 porphyrin toward azides, and the small amount of reactive A_2B_2 porphyrins present, purification of *m*-alkynyl−ZnP **3** and *p*-alkynyl−ZnP **4** by column chromatography was only carried out on a small scale (see Experimental Section). The purified A_3B alkynyl porphyrins were used for yield determinations, spectral analysis, and photophysical studies.

Meta- and *para*-azidobenzaldehydes (**5** and **6**, respectively) were synthesized by reacting the corresponding bromobenzaldehydes with sodium azide, copper iodide, sodium ascorbate, and *N*,*N*′-dimethylethylenediamine according to a published procedure.[28] The progress of the reaction was monitored by the appearance of the characteristic azide absorption band near 2100 cm^{-1} in the Fourier-transform IR (FTIR) spectrum (see Figure S1, Supporting Information).

The CuAAC between alkynylporphyrins and azidobenzaldehydes was performed under microwave irradiation. An argon-purged solution of alkynyl porphyrins **3** or **4**, azides **5** or **6**, copper iodide, and sodium ascorbate in 9:1 dimethylsulfoxide/water ($DMSO/H_2O$) was heated in a microwave reactor (80 °C, 50 W) for 30 min. Standard workup (see Experimental Section) and column chromatography provided pure ZnP−Tri products—*m*4*m* (**7**), *m*4*p* (**8**), and *p*4*p* (**9**)—in yields ranging from 9% to quantitative. Since the yield of **9** in the uncatalyzed reaction was low (9%), a reaction was carried out between **4** and **6** in the presence of 1 equiv of the additive tris(benzotriazolylmethyl)amine (TBTA),[29] whereupon the yield of **9** improved from 9% to 40%.

The ZnP−Tri adducts were characterized by MALDI-TOF mass spectrometry and ^1H NMR. Mass spectra display peaks for the molecular ion and M-28 resulting from loss of nitrogen (Figure S2, Supporting Information). The most significant changes in the NMR spectra are the appearance of a singlet at 8.3−8.6 ppm (proton on triazole ring) and the disappearance of the singlet at 3.1−3.3 ppm (alkynyl proton) (Figure 4).

The synthesis of *p*-azidophenylporphyrin[30] (**12**) also utilized the Lindsey mixed-aldehyde method, substituting *p*-acetamidobenzaldehyde for ethynylbenzaldehyde (**1**). The resulting *p*-acetamidophenylporphyrin[31] (**10**) was hydrolyzed[32] to the *p*-aminophenylporphyrin (**11**), which was then converted using sodium nitrite and sodium azide, via the diazonium salt, to the *p*-azidophenylporphyrin (**12**). This porphyrin and either *p*- or *m*-ethynylbenzaldehyde[33] (**13** or **14**) were then used in a microwave-assisted CuAAC in the presence of TBTA[29] to afford *p*1*p*- or *p*1*m*-ZnP−tri-benzaldehyde (**15** or **16**) in 84% yields.

Finally, the ZnP−Tri−C_{60} conjugates **17**−**21** were synthesized by the Prato 1,3-dipolar cycloaddition to C_{60} of the azomethine ylides derived from the respective porphyrin-triazole-benzaldehydes and sarcosine. The first Prato reactions attempted followed the conditions of the standard references[26] using 1 equiv of C_{60} for every 2 equiv of aldehyde. Thin-layer chromatography (TLC) showed complete consumption of C_{60}, but the conjugates showed similar R_f as the ZnP−Tri precursors, causing difficulties in isolating the desired conjugates. Changing to 2 equiv of C_{60} for every equivalent of the aldehyde provided two major benefits: (1) chromatographic purification from the excess C_{60} was made easier by requiring only one short column rather than multiple long columns, saving time and resources, and (2) the product yield was doubled as the less available ZnP−Tri precursor became the limiting reagent. The ZnP−triazole−fulleropyrrolidine products

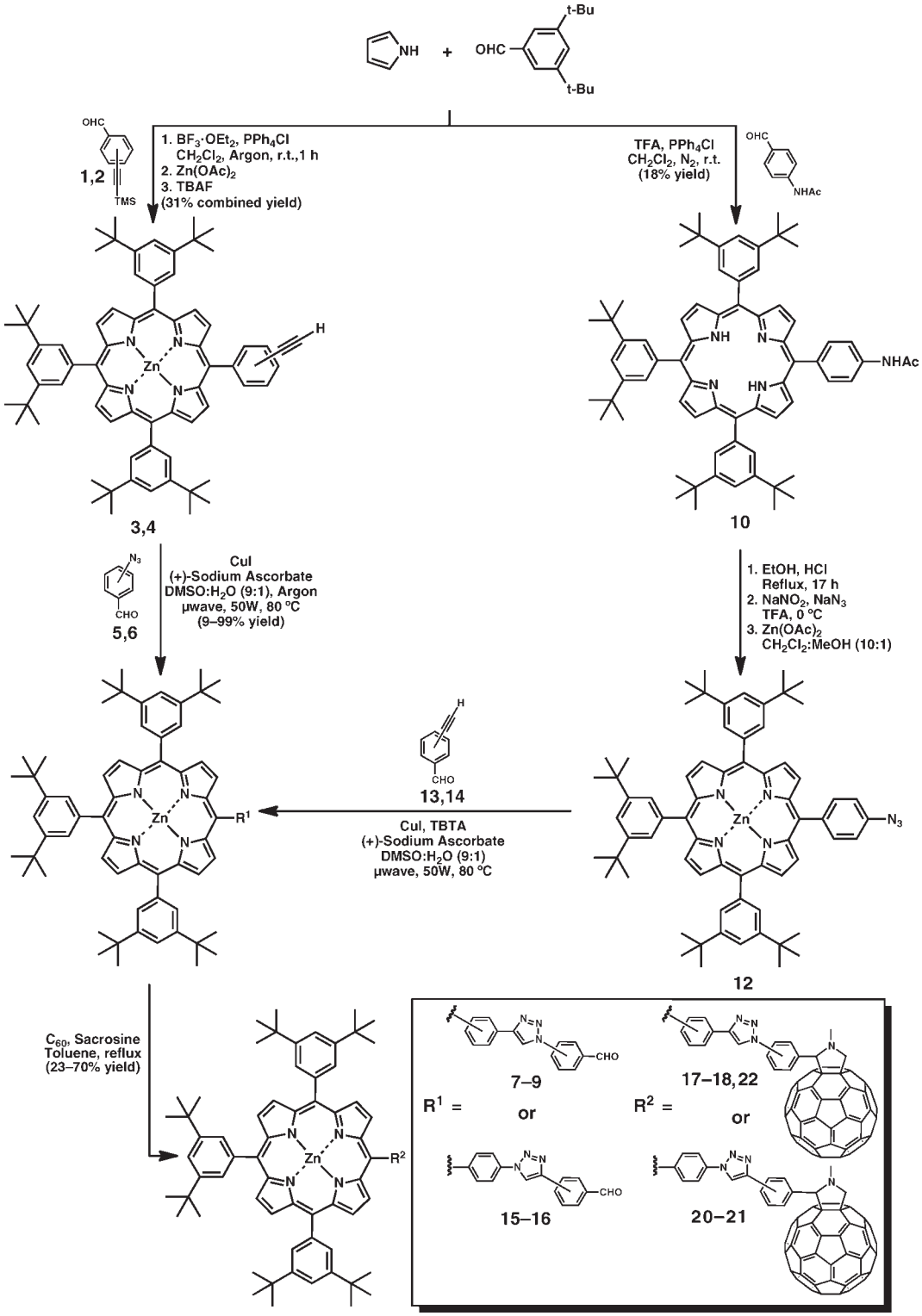

Figure 3. General scheme for the synthesis of *m*4*m*-, *m*4*p*-, *p*4*p*-, *p*1*p*-, *p*4*m*-, and *p*1*m*-ZnP−Tri−C_{60} conjugates.

were characterized by MALDI-TOF mass spectrometry, which showed peaks for the conjugates minus N_2[34] and for the conjugates minus C_{60} + N_2 (Figures S3, S4, and S5, Supporting Information), ^{1}H NMR (Figures S7, S8, and S9, Supporting Information), and correlation spectroscopy (COSY) NMR (Figure 5 and Figures S10 and S11, Supporting Information).

The assignment of peaks in the ^{1}H NMR spectrum of *m*4*m*-ZnP−Tri−C_{60} (**17**) (Figure S6, Supporting Information) was aided by its COSY NMR spectrum (Figure 5) by first assigning peaks to the simpler *p*4*p*-ZnP−Tri−C_{60} (**19**) (Figures S9 and S11, Supporting Information). It was then possible to make assignments in the more complicated NMR spectrum of

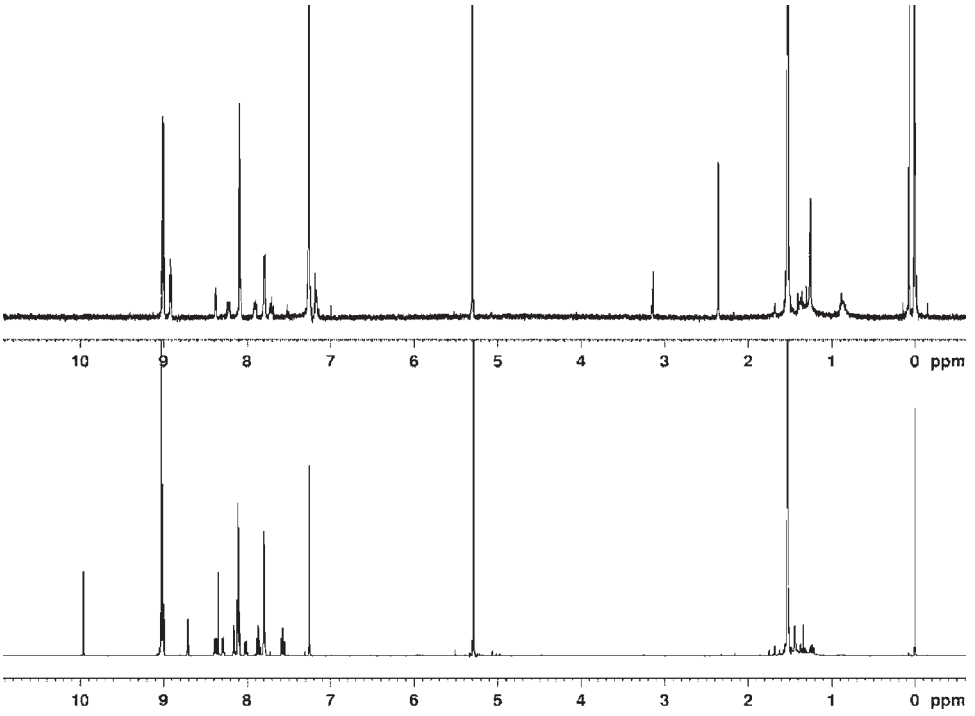

Figure 4. Top: ^{1}H NMR spectrum of *m*-alkynyl−ZnP (**3**). The ethynyl proton appears at 3.1 ppm. Bottom: ^{1}H NMR spectrum of *m*4*m*-ZnP−Tri (**7**). The triazole proton appears at 8.35 ppm.

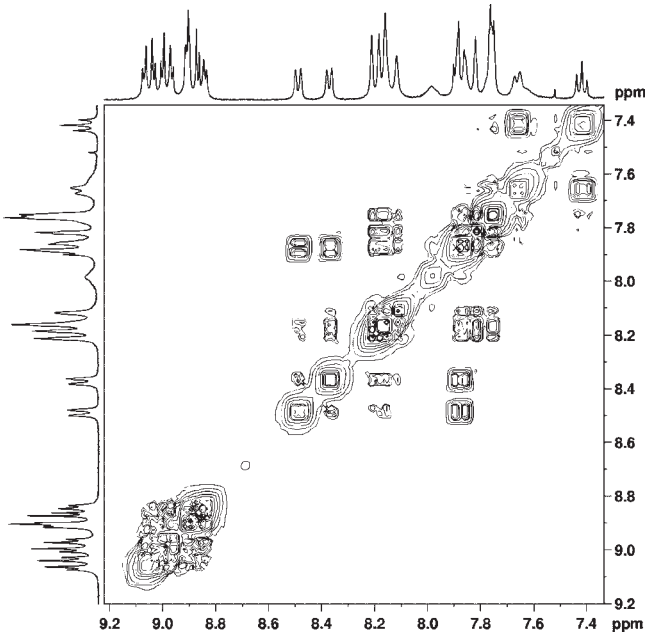

Figure 5. COSY ^{1}H NMR spectrum of *m*4*m*-ZnP−Tri−C_{60} **17** in $CDCl_3$.

*m*4*p*-ZnP−Tri−C_{60} (**18**) (Figures S8 and S10, Supporting Information), aided by its COSY spectrum, in which similar chemical shifts are observed for protons on the *meta*-substituted phenyl ring on the porphyrin. The *m*4*m*-ZnP−Tri−C_{60} ^{1}H NMR spectrum also shows better resolution of the β-porphyrinic protons (8.8−9.1 ppm) than was observed in the other conjugates and their precursors.

2. Theoretical Calculations. Molecular modeling provides strong evidence favoring a through-bond electron transfer (ET) mechanism via the triazole linker in all but one of the ZnP−Tri−C_{60} conjugates. As a first step, it was important to ascertain whether through-space interactions in **17**−**22** are feasible due to their structural properties. Thus, the geometries of the six different conjugates were optimized, and the center-to-center donor−acceptor distances were determined. Since the structural flexibility of the molecules rendered it difficult to obtain reasonable starting geometries, the initial molecular models were constructed with the shortest possible donor−acceptor distance with respect to the van der Waals radii of the atoms. These geometries were then relaxed using different quantum chemical optimization methods involving semiempirical calculations and density functional theory (DFT). For semiempirical calculations, the PM3[35] and AM1[36] Hamiltonians were used. The DFT calculations were performed using the M062X[37] functional and the 6-31G*[38] basis set with LANL2DZ[39] pseudopotentials on the zinc atoms. Superpositioning the geometries obtained by the different computational methods resulted in root-mean-square deviation (rmsd) values between 0.11 and 0.36 Å, which represents a very good match between the PM3, AM1, and M062X structures. The center-to-center distances obtained at the different levels of calculations for all geometries varied in the range of ≤0.5 Å (Table 1).

In cases where the distance between donor and acceptor moieties is small enough to allow for direct overlap between the frontier orbitals of the donor and acceptor, ET may occur by a through-space mechanism. When the donors and acceptors are too far apart for direct orbital overlap to be significant, ET may occur via a superexchange or hopping mechanism governed by through-bond interactions. Diffusionless through-space ET is known to occur at distances of 4−10 Å since only then are the electron donors and acceptors close enough to allow for efficient

Table 1. Calculated Center-to-Center Distances in Å between ZnP and C_{60} as Computed by Different Computational Methods

	m4m-ZnP−Tri−C_{60} **17**	*m4p*-ZnP−Tri−C_{60} **18**	*p1m*-ZnP−Tri−C_{60} **21**	*p1p*-ZnP−Tri−C_{60} **20**	*p4m*-ZnP−Tri−C_{60} **22**	*p4p*-ZnP−Tri−C_{60} **19**
AM1	10.57	14.34	16.01	18.91	15.33	18.59
PM3	10.88	14.83	16.10	19.05	15.29	18.84
M062X	9.78	14.33	16.69	19.37	15.32	19.12

Table 2. Calculated Orbital Energies in eV (M062X/6-31G*//LANL2DZ) of the ZnP−Tri−C_{60} Conjugates, ZnP and C_{60}

	ZnP	C_{60}	*m4m*-ZnP−Tri−C_{60} **17**	*m4p*-ZnP−Tri−C_{60} **18**	*p1m*-ZnP−Tri−C_{60} **21**	*p1p*-ZnP−Tri−C_{60} **20**	*p4m*-ZnP−Tri−C_{60} **22**	*p4p*-ZnP−Tri−C_{60} **19**
HOMO-4	−8.0	−7.5	−7.1	−7.1	−7.0	−7.0	−7.2	−7.1
HOMO-3	−8.0	−7.1	−7.1	−7.1	−7.0	−6.9	−7.1	−7.1
HOMO-2	−8.0	−7.0	−6.6	−6.6	−6.5	−6.4	−6.6	−6.6
HOMO-1	−6.1	−7.0	−6.1	−6.1	−6.2	−6.2	−6.1	−6.1
HOMO	−6.0	−6.5	−5.9	−5.9	−6.1	−6.1	−5.9	−5.9
LUMO	−1.7	−3.0	−3.1	−3.0	−3.0	−2.9	−3.1	−3.1
LUMO+1	−1.7	−2.6	−2.7	−2.6	−2.6	−2.5	−2.7	−2.7
LUMO+2	0.3	−2.3	−2.4	−2.4	−2.3	−2.3	−2.5	−2.4
LUMO+3	0.8	−1.7	−1.8	−1.7	−1.8	−1.8	−1.8	−1.8
LUMO+4	0.8	−1.2	−1.7	−1.7	−1.8	−1.8	−1.6	−1.7

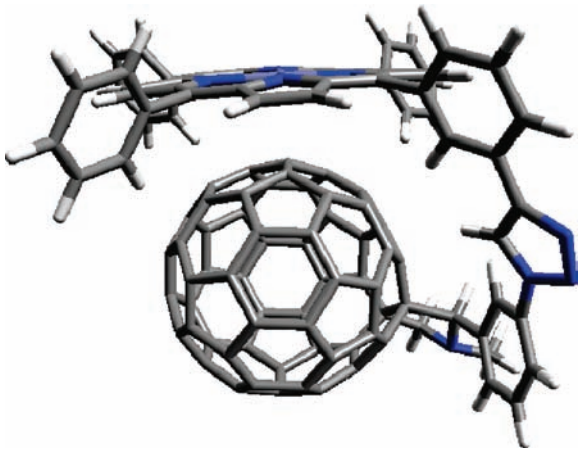

Figure 6. Optimized geometry of the *m4m*-ZnP−Tri−C_{60} conjugate **17** resulting from DFT calculations.

orbital overlap. Such a situation is feasible only in *m4m*-ZnP−Tri−C_{60} **17** with its face-to-face arrangement (see Figure 6). In all the other conjugates, the configuration of the bridge does not allow donor−acceptor distances to be closer than 14 Å. Hence, through-space ET is likely to occur only in **17**, while in all other systems through-bond ET dominates.

The analysis of molecular orbitals (MOs) confirms the donor−acceptor character of the ZnP−Tri−C_{60} conjugates. In all systems, the highest occupied MO (HOMO) is localized on the ZnP donor and the lowest unoccupied MO (LUMO) on the C_{60} acceptor. Importantly, the energies of the orbitals depend on (1) the positions of nitrogen in the triazole ring and (2) the substitution pattern at the bridge, that is, *meta* vs *para* (Table 2). In particular, the HOMO energy is higher (−5.9 eV) when the ZnP moiety is attached to the C atom of the triazole ring and not to the N atom (−6.1 eV), e.g., *p1m*-ZnP−Tri−C_{60} (**21**) vs *p4m*-ZnP−Tri−C_{60} (**22**) and *p1p*-ZnP−Tri−C_{60} (**20**) vs *p4p*-ZnP−Tri−C_{60} (**19**). On the other hand, higher LUMO energies (−2.9 eV) were found for the conjugates in which the ZnP moiety is attached to the N atom rather than the C atom (−3.1 eV) of the triazole. The variation of the HOMO/LUMO gap goes along with the differences in ground-state conjugation imposed by the variation of the connectivity pattern at the triazoles. Lowering the HOMO/LUMO gap increases the electronic coupling, which, in turn, increases the charge transfer in the conjugates. In general, the HOMO−LUMO gaps scale linearly with the donor−acceptor distance.

As noted above, through-space orbital overlap in *m4m*-ZnP−Tri−C_{60} **17** is present due to the donor−acceptor proximity. Thus, HOMO coefficients are found not only on ZnP but also on C_{60} (Figure 7).

Local electron affinity (EA) and semiempirical excited state configuration interaction (CI) calculations were used to account for the variation of ET rates in the ZnP−Tri−C_{60} conjugates. The photophysical studies to be discussed below confirm the formation of radical ion pairs in all six systems. Charge separation and charge recombination rates in all but one of the conjugates varied with the dielectric constant (molecular permittivity) of the solvent, as expected for a through-bond ET process. Through-space ET processes lack such a solvent dependence, as seen for the *m4m* conjugate. The through-bond donor−acceptor distance, as determined from the bond lengths, is invariant in all of the ZnP−Tri−C_{60} conjugates. Hence, the variation of the connectivity pattern on the triazole ring imposes different structural arrangements of the bridge moieties, which impact the through-bond electronic coupling. In general, *meta* as opposed to *para* connectivity imposes bending of the bridge and favors a conformation in which ZnP is in closer proximity to C_{60}. The variation of the nitrogen atom positions in the triazole moiety, that is, whether ZnP is attached at position 1 (nitrogen)

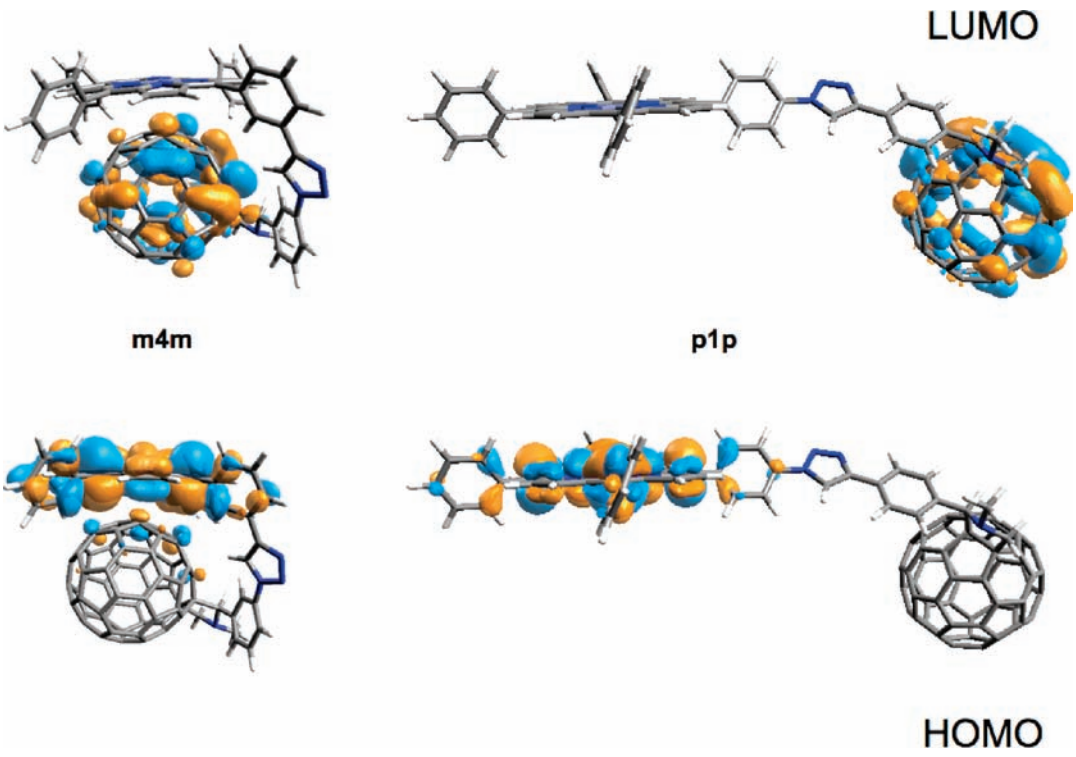

Figure 7. Coefficients of the HOMO (bottom) and LUMO (top) of *m*4*m*-ZnP−Tri−C_{60} (**17**) and *p*1*p*-ZnP−Tri−C_{60} (**20**) as computed by DFT methods, demonstrating through-space interactions in **17**.

or position 4 (carbon), affects the electronic properties of the bridge. Local EA calculations provided insight into these findings. EA maxima are found on all nitrogen atoms (Figure S12, Supporting Information), and a homogeneous ET pathway through the bridge is found in all of the conjugates. However, the pronounced local EA maxima on the nitrogens suggest that the triazoles are, to some extent, electronically isolated and may function as intermediate electron acceptors. Nevertheless, C_{60} remains the ultimate electron acceptor as seen from the color code, and the triazoles may serve to lower the charge injection barrier into the bridge.

A pathway of high EA values can only be realized in the presence of homogeneous π-conjugation, which again favors through-bond interactions (Figure S12, Supporting Information). To analyze the structural differences in ZnP−Tri−C_{60} conjugates **17**−**22** quantitatively, we have compared the local EA values on the triazole rings in the six different configurations. Interestingly, with *meta*-connectivity and ZnP attachment to the triazole carbon, the EA values on the triazole ring increase as compared to *para*-connectivity or ZnP attachment to the triazole nitrogen (Table S1, Supporting Information).

The results of the theoretical studies agree nicely with the accelerated electron transfer dynamics found in the photophysical studies described below. With higher EA at the triazole sites, lower energy states are available. These energy states may be occupied by the electrons to be transferred, facilitating through-bond ET by lowering the charge injection barrier. When the C_{60} is connected to the triazole nitrogen, higher EA values appear on the carbon atom directly connected to the ZnP, as compared to the alternative pattern (see Figure S12, Supporting Information). Such a situation provides favorable coupling between the triazole and the adjacent phenyl ring on the porphyrin, resulting in accelerated ET. Thus, the electron-accepting features may affect the lone pair electrons of the substituted nitrogen atom and induce electron deficiency at the adjacent carbon. CI calculations were performed to corroborate these findings. It was possible to determine the energies of the charge-transfer (CT) states for all ZnP−Tri−C_{60} conjugates. Analysis of their heats of formation in relation to the ground state as a function of donor−acceptor distance results in a linear relationship (Figure S13, Supporting Information). Higher dipole moments are induced at larger through-bond donor−acceptor distances, leading to increased activation barriers for the formation of the radical ion pair and, hence, to higher values of ΔH_f. This underlying dependence reflects the trends of the charge transfer rate constants determined in the photophysical studies.

Imaging the electrostatic potentials of the CT states on the van der Waals surface of the molecules corroborates the findings of the local EA investigations, namely, the electron-accepting features of the triazole units. In all systems, the positive charge resides on the ZnP moiety, while the negative charge is partially distributed over the C_{60} framework and the triazole atoms. Calculation of the partial charges on these residues indicates that the ZnP accommodates +1.1 e^-, whereas −0.3 e^- and −0.6 e^- reside on the triazoles and C_{60}, respectively. Thus, the higher the EA value on the nitrogen atoms, the more charge they can accommodate. These results suggest that the triazole may serve as a secondary electron acceptor in these systems, which is further confirmed by considering additional excited states. Bridge charge transfer (BCT) states of true CT character were discovered by calculations including the solvent (Figure 8). With increasing solvent polarity, their energies decrease, as shown in Figure S14 (Supporting Information). In all these BCT states, the positive charge is located on both C_{60} and the triazole.

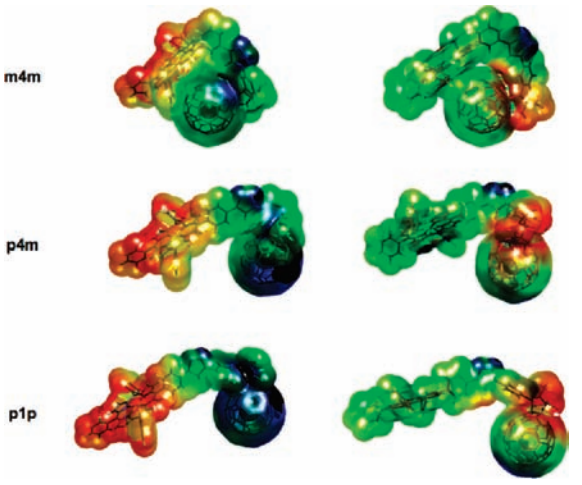

Figure 8. Molecular electrostatic potentials (red to blue: positive to negative) from CI calculations for the CT (left) and BCT (right) states of *m*4*m*-ZnP−Tri−C_{60} (**17**), *p*4*m*-ZnP−Tri−C_{60} (**22**), and *p*1*p*-ZnP−Tri−C_{60} (**20**).

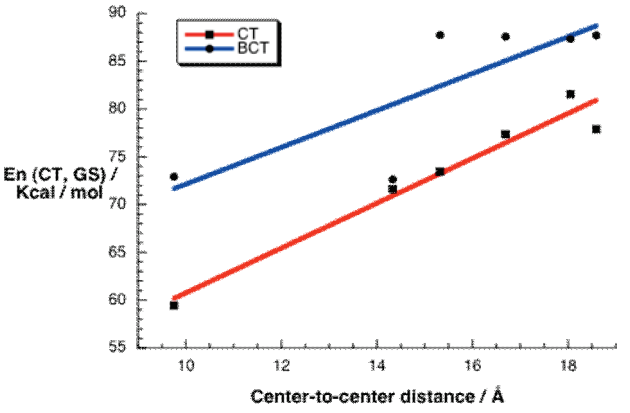

Figure 9. Energy difference between the CT and BCT states and the ground state as a function of donor−acceptor distance, as determined from CI calculations, shows increasing mixing between CT and BCT states upon increasing the donor−acceptor distance.

Figure 9 shows that with increasing donor−acceptor distance the energies of the BCT and CT states approach each other, suggesting mixing of these states with increasing distance upon photoexcitation. In this situation, BCT states may act as traps and, depending on their energies, provide an alternative CT pathway. When the BCT states are energetically well-separated from the CT states, photoexcitation will result in direct population of the CT state (Figure 8, left); however, when the energies of the BCT and CT states approach each other, the "true" CT state results from a mixing of the CT (Figure 8, left) and BCT (Figure 8, right) electronic distributions. In such cases, the CT mechanism involves localization of charge on the linker, which decelerates the charge separation and also the charge recombination processes.

Thus, the CI calculations clearly demonstrate that ET occurs quite efficiently but depends on the substitution pattern on the triazole ring. Connecting the phenyl moieties at different positions at the triazole impacts the ground-state conjugation, as reflected by the variation of the HOMO and LUMO energies.

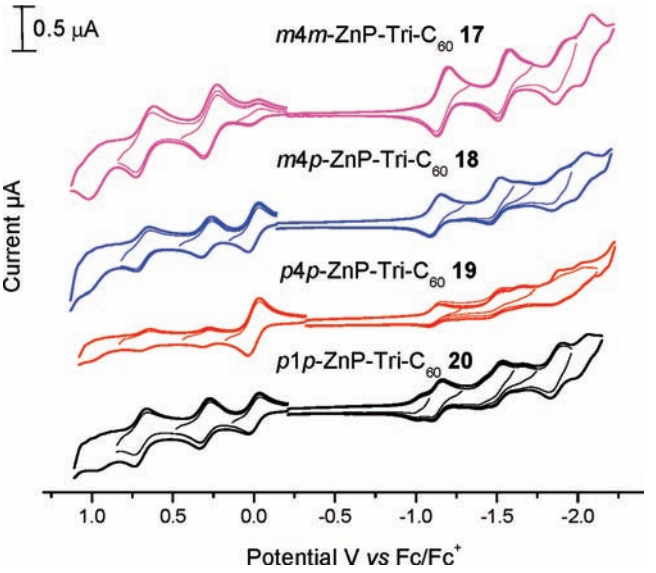

Figure 10. Cyclic voltammograms of ZnP−Tri−C_{60} conjugates **17**−**20** in dichloromethane containing $TBAPF_6$ (0.1 mol dm^{-3}) with a sweep rate of 100 mV s^{-1}.

Because of the weak conjugation in the ground state, HOMO and LUMO energies remain close to those of the individual ZnP and C_{60} energies, as shown in Table 2. Correlation between these findings and the EA and CI calculations suggests that the most efficient ET occurs when the electronic perturbation in the excited state does not affect the conjugation and the electronic coupling in the ground state. Attaching ZnP directly to the triazole nitrogen interrupts the conjugation because the CT resonance structure has cationic character due to formation of a quaternary ammonium center.[40] This break in conjugation is reflected by the mixing of BCT and CT states. Despite the fact that *para*-connectivity provides more efficient electronic coupling in the ground state, *meta*-connectivity may improve the charge separation features due to enhanced through-space coupling induced by the significantly shorter donor−acceptor distances.

3. Electrochemical Studies: Study of Ground State Interactions. The redox properties of ZnP−Tri−C_{60} conjugates (**17**−**20**), ZnP−Tri references (**7**, **8**, **9**, **15**, and **16**), and reference compound alkynyl porphyrins **3** and **4** were studied by means of differential pulse voltammetry (DPV) and cyclic voltammetry (CV). The measurements were carried out in anhydrous dichloromethane (DCM) using tetra-*n*-butylammonium hexafluorophosphate ($TBAPF_6$) as the supporting electrolyte and ferrocene/ferrocinium (Fc/Fc^+) as the internal reference. The half-wave potentials, $E_{1/2}$, were determined as $(E_{pa} + E_{pc})/2$, where E_{pa} and E_{pc} are the anodic and cathodic peak potentials determined from the CV measurements. All potentials obtained from DPV were converted to $E_{1/2}$ values using the formula $E_{max} = E_{1/2} - (\Delta E/2)$, where ΔE is the pulse amplitude (50 mV).[41]

Figure 10 and Figure S15 (Supporting Information) show the CV and DPV data for ZnP−Tri−C_{60} conjugates **17**−**20**.[42] Each of these compounds shows two reversible one-electron oxidation processes. The first oxidation peak is attributed to the ZnP group (**7**−**9** and **15**), which was shifted cathodically (70, 10, 10, and 20 mV for compounds **17**, **18**, **19**, and **20**, respectively, compared to the ZnP references **3** and **4**). On the reduction side, the materials exhibit at least four peaks each.

Table 3. Electrochemical Potentials E/V vs Fc/Fc^+ Measured in Dichloromethane Containing $TBAPF_6$ (0.1 mol dm^{-3}) as Supporting Electrolyte

	reduction potentials (V)							oxidation potentials (V)		
compound	E^1	E^2	E^3	E^4	E^5	E^6	E^7	E^1	E^2	HOMO−LUMO[b](V)
m-ZnP **3**					−1.87[a]		−2.22	0.32[a]	0.68[a]	2.19
p-ZnP **4**					−1.87[a]		−2.22	0.29[a]	0.69[a]	2.16
2-NMFP **23**[43a]		−1.07[a]	−1.45[a]		−1.98[a]					
*m*4*m*-ZnP−Tri **7**					−1.84[a]	−2.15		0.30[a]	0.67[a]	2.14
*m*4*p*-ZnP−Tri **8**					−1.86[a]	−2.10		0.30[a]	0.65[a]	2.16
*p*4*p*-ZnP−Tri **9**					−1.85[a]	−2.09	−2.24	0.31[a]	0.67[a]	2.16
*p*1*p*-ZnP−Tri **15**					−1.81[a]	−2.18		0.33[a]	0.66[a]	2.14
*m*4*m*-ZnP−Tri−C_{60} **17**		−1.16[a]	−1.54[a]		−1.93	−2.08		0.23[a]	0.67[a]	1.39
*m*4*p*-ZnP−Tri−C_{60} **18**		−1.12[a]	−1.49[a]		−1.90	−2.02		0.29[a]	0.69[a]	1.41
*p*4*p*-ZnP−Tri−C_{60} **19**		−1.12[a]	−1.49[a]	−1.67	−1.90	−2.04		0.30[a]	0.68[a]	1.42
*p*1*p*-ZnP−Tri−C_{60} **20**	−1.02	−1.13[a]	−1.54	−1.67	−1.87[a]	−2.07		0.31[a]	0.70[a]	1.44
24[43b]		1.07[a]	−1.45[a]		−1.82[a]	−1.99		0.34[a]	0.69[a]	1.41

[a] Denote $E_{1/2}$ potentials. Range 60−92 mV of anodic-to-cathodic peak separation. [b] HOMO−LUMO: $\Delta E = E_1{}^{st}{}_{oxidation} - E_1{}^{st}{}_{reduction}$.

The first and the second reversible one-electron reductions correspond to the fulleropyrrolidine moiety, while the third irreversible one-electron reduction appears to be centered on ZnP, based on the values obtained for the ZnP and ZnP−Tri references (Figure S16, Supporting Information, and Table 3). Considering the structure of compounds **17**−**20**, in which the triazole group is connected to the carbon of the pyrrolidine ring, the first reduction potential of each conjugate was compared with the well-known *N*-methyl-2-pyridylfulleropyrrolidine **23** reported previously (Figure S17, Supporting Information).[43a] The potential had shifted cathodically compared with the first reduction potential (−1.07 V) of **23** (90, 50, 50, and 60 mV for compounds **17**, **18**, **19**, and **20**, respectively). This shift indicates that the conjugates are slightly harder to reduce than **23**.[43a] The third reduction peak for **17**, **18**, **19**, and **20** was shifted cathodically by 90, 40, 50, and 60 mV, respectively, with respect to the corresponding ZnP−Tri references. This cathodic shift can be assigned to the electronic coupling between C_{60} and the porphyrin. The two extra reduction peaks in the DPV of **20** (Figure S15, Supporting Information) are unassigned and may be due to contamination with a small amount of pristine C_{60}. The CV and DPV curves for **17**−**20** closely correspond to the sum of the independent electrochemical features of the individual C_{60} and ZnP moieties with some potential value shifts as described above.

Table 3 reports all the electrochemical potentials for this series of ZnP−Tri−C_{60} conjugates and the corresponding reference compounds. It can be observed that the HOMO−LUMO gaps of all conjugates are similar (1.39−1.44 V) and in the range (1.41 V) previously reported for azobenzene-linked porphyrin−fullerene dyad **24** (Figure S17, Supporting Information).[43b]

4. Photophysical Properties: Study of Excited State Interactions. *4.1. Absorption Spectroscopy.* To provide insight into possible ground state electronic interactions between the photo- and redox-active moieties, namely, ZnP and C_{60}, the absorption spectra of the ZnP−Tri−C_{60} conjugates **17**−**22** were compared with those of the individual constituents. The dominating Soret- and Q-bands of ZnP are seen in the 400−450 nm and 550−650 nm regions, respectively, while the strongest C_{60} bands appear at 220, 265, and 330 nm and extend all the way to the energetically lowest-lying transition at 690 nm (see Figure 12). With the exception of *m*4*m*-ZnP−Tri−C_{60} **17**, the absorption spectra of the conjugates are best described as simple superimpositions of the component spectra, lacking notable perturbations or additional charge transfer transitions (see Figure S18, Supporting Information). These results indicate that no significant interchromophoric interactions exist in the electronic ground state of these conjugates.

A close inspection of the Soret band of *m*4*m*-ZnP−Tri−C_{60} **17** in toluene shows 2 nm red-shift along with peak broadening (Figure 11). These spectral changes are also evident in the more polar solvents THF and PhCN. A comparison of the Q-band regions of *m*4*m* conjugate **17** and *m*4*m*-ZnP−Tri **15** revealed no new absorption bands in the case of **17**. Consequently, formation of a charge transfer (CT) state between ZnP and C_{60} accounts for the Soret band changes in the *m*4*m* conjugate, although the absence of a detectable CT absorption band suggests rather weak electronic coupling. The shorter distance between ZnP and C_{60} in *m*4*m*-ZnP−Tri−C_{60} **17**, ∼10 Å, compared to the other conjugates, >14 Å, facilitates electronic interaction in the ground state. This trend resembles that of previously reported similar short-distance porphyrin−fullerene hybrids,[24a,44] in which donor−acceptor separations shorter than 10 Å are crucial for CT state formation.

4.2. Fluorescence Spectroscopy. Fluorescence studies were carried out with the ZnP−Tri−C_{60} conjugates **17**−**22** in solvents of different polarity (i.e., toluene, THF, and benzonitrile) using solutions with identical optical density (0.2) at the excitation wavelengths of 425 and 432 nm. The conjugates and the ZnP−Tri references exhibit fluorescence maxima at 599/648 nm in toluene, 602/655 nm in THF, and 610/665 nm in benzonitrile (see Figure 12 for the spectra of *p*1*m* conjugate **21**). The fluorescence quantum yields of the ZnP−Tri references (Φ_f = 0.04) are invariant in these three solvents. In the ZnP−Tri−C_{60} conjugates, the ZnP fluorescence is significantly quenched, with quantum yields ranging from 0.0017 to 0.0085 (for details see Table 4), which translates to quenching factors of up to 23 compared to the ZnP reference compounds. Although the ZnP−Tri−C_{60} conjugate quantum yields decrease, the ZnP emission patterns are not affected by the presence of the electron-accepting C_{60} moiety (Figure 12, lower).

Finally, the near-infrared region was probed in terms of possible CT emissions. Only for *m*4*m*-ZnP−Tri−C_{60} (**17**) and only in

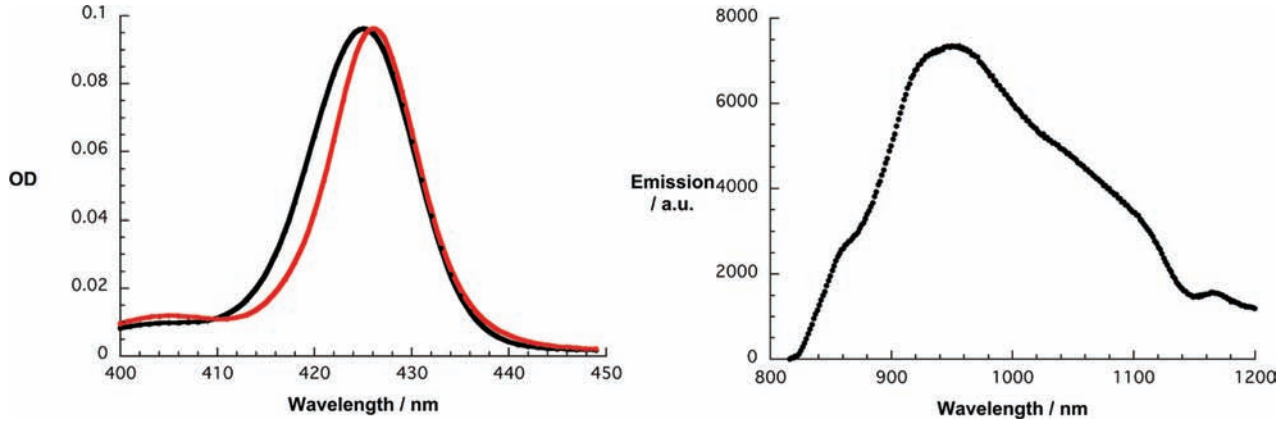

Figure 11. Absorption (left) spectra of *m*4*m*-ZnP−Tri **7** (black line) and *m*4*m*-ZnP−Tri−C_{60} **17** (red line) and emission (right) spectra of **17** in toluene.

Table 4. Photophysical Data of ZnP−Tri−C_{60} Conjugates in Solution at Room Temperature

feature	solvent	*m*4*m*-ZnP−Tri−C_{60} **17**	*m*4*p*-ZnP−Tri−C_{60} **18**	*p*1*p*-ZnP−Tri−C_{60} **20**	*p*4*p*-ZnP−Tri−C_{60} **19**	*p*4*m*-ZnP−Tri−C_{60} **22**	*p*1*m*-ZnP−Tri−C_{60} **21**
$\Phi_f \times 10^3$	toluene	2.6	7.5	6.6	4.1	1.7	4.7
	THF	3.0	8.5	4.0	2.2	1.7	4.9
	BzCN	3.2	8.5	3.7	2.4	1.7	4.7
τ_f [ns]	toluene	0.24	0.32	0.39	0.25	0.12	0.25
	THF	0.20	0.31	0.19	0.20	0.18	0.12
	BzCN	0.22	0.36	0.20	0.21	0.10	0.13
k_{cs} [s^{-1}] $\times 10^9$ [a]	toluene	6.3	1.9	2.2	3.8	9.8	3.3
	THF	5.4	1.6	3.9	7.5	9.8	3.1
	BzCN	5.0	1.6	4.2	6.8	9.8	3.3
τ_s [ns]	toluene	0.25	0.34	0.42	0.20	0.08	0.11
	THF	0.20	0.24	0.17	0.10	0.05	0.06
	BzCN	0.09	0.08	0.09	0.09	0.05	0.07
k_{cs} [s^{-1}] $\times 10^9$ [b]	toluene	3.6	2.5	1.9	4.6	12.1	8.7
	THF	4.6	3.7	5.5	9.6	19.6	16.2
	BzCN	10.7	12.1	10.7	10.7	19.6	13.9
τ_{csrp} [ns]	THF	418	522	844	645	419	656
	BzCN	420	440	646	560	405	485
k_{cr} [s^{-1}] $\times 10^{-6}$	THF	2.4	2.2	1.2	1.5	2.4	1.5
	BzCN	2.4	2.4	1.5	1.8	2.5	2.1

[a] k_{cs} was determined from the fluorescence quantum yields via

$$k_{cs} = [\Phi_{(reference)} - \Phi_{(conjugate)}]/[\tau_{(reference)}\ \Phi_{(conjugate)}] \quad (1)$$

[b] k_{cs} was determined from the time decay curves via

$$k_{cs} = 1/\tau_{(conjugate)} - 1/\tau_{(reference)} \quad (2)$$

toluene was a CT-type emission detected (see Figure 11). The aforementioned results corroborate the absence of interactions between ZnP and C_{60} in the ground state. For **17**, the fact that the CT emission band was only detected in toluene suggests very weak coupling between the active units. CT emission has been reported to occur in ZnP−C_{60} conjugates with similar donor−acceptor distances in a variety of solvents,[24a,44] which suggests that the particular orientation of the components in our ZnP−Tri−C_{60} conjugates might prevent the formation of CT states.

Changing the solvent polarity from toluene (ε = 2.38) via THF (ε = 7.6) to benzonitrile (ε = 24.8) leads to intensification of the fluorescence quenching, particularly for *p*1*p*-ZnP−Tri−C_{60} (**20**) and *p*4*p*-ZnP−Tri−C_{60} (**19**), while the remaining conjugates exhibit much weaker dependence on solvent polarity. The sizable fluorescence quenching and its trend as a function of solvent polarity for **20** and **19** are attributed to an intramolecular ET process. Thus, the latter must occur through the connecting bridge since the center-to-center distances between the ZnP and C_{60} moieties in the most stable conformations of these conjugates

dx.doi.org/10.1021/ja202485s |*J. Am. Chem. Soc.* 2011, 133, 13036–13054

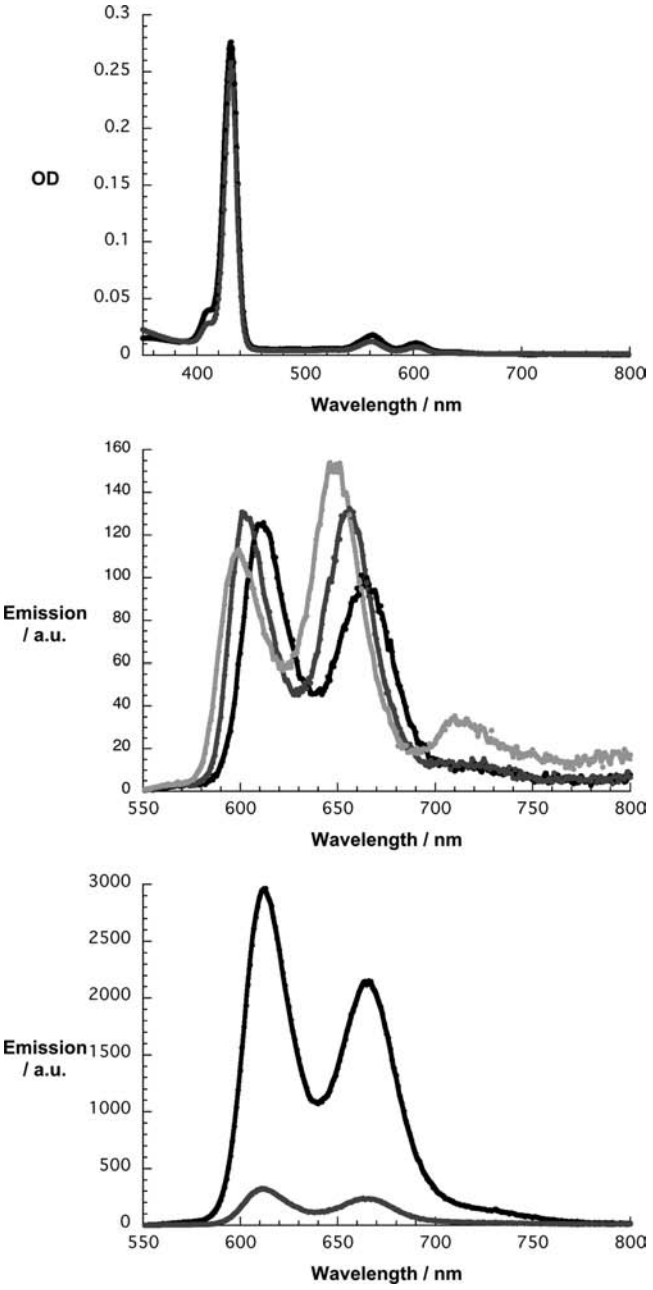

Figure 12. Top: absorption spectra at 298 K of *p*1*m*-ZnP−Tri **16** (black line) and *p*1*m*-ZnP−Tri−C_{60} **21** (gray line) in benzonitrile. Middle: fluorescence spectra at 298 K of *p*1*m*-ZnP−Tri−C_{60} **21** in toluene (light gray lines), THF (dark gray line), and benzonitrile (black line), λ_{exc} = 425 nm. Bottom: fluorescence spectra at 298 K of *p*4*p*-ZnP−Tri **9** (black line) and *p*4*p*-ZnP−Tri−C_{60} **19** (gray line) in benzonitrile, λ_{exc} = 432 nm.

exceed 10 Å, preventing a direct through-space ET process. Only in *m*4*m*-ZnP−Tri−C_{60} (**17**), where the center-to-center distance barely reaches 10 Å (vide supra), is a through-space ET process possible. However, the possibility that a through-bond ET may also occur to some extent in **17** cannot be excluded.

In toluene, all ZnP−Tri−C_{60} conjugates feature a weak fluorescence maximum at 710 nm, corresponding to emission from the C_{60} singlet excited state, which indicates transduction of singlet excited state energy from ZnP to C_{60}. In this solvent, deactivation by intramolecular energy transfer (EnT) competes with charge separation (ET). Such an energy transfer scenario leads to the most intense C_{60} fluorescence in the case of *p*4*m*-ZnP−Tri−C_{60} (**22**), possibly due to a particularly favorable orientation of the dipole moments since the center-to-center distance is midrange.

Based upon the relationship between the fluorescence quantum yields in the conjugates ($\Phi_{(conjugate)}$), the fluorescence quantum yields of ZnP ($\Phi_{(reference)}$), and the fluorescence lifetimes of the ZnP's ($\tau_{(reference)}$), one can determine the rate constants for fluorescence deactivation (Table 4). In general, the rates are extremely fast, indicating strong electronic coupling between the donors and acceptor moieties. The relationship between charge separation rates and structure is interesting. Larger k_{cs} values were observed for the ZnP−Tri−C_{60} conjugates with ZnP linked to the C atom of the triazole ring, namely, *p*4*m*-ZnP−Tri−C_{60} (**22**) and *p*4*p*-ZnP−Tri−C_{60} (**19**), than in the corresponding conjugates with ZnP linked to the N atom, *p*1*m*-ZnP−Tri−C_{60} (**21**) and *p*1*p*-ZnP−Tri−C_{60} (**20**), respectively. Thus, the connectivity pattern between ZnP and C_{60} strongly affects the rates of charge separation in these conjugates.

The magnitude of ET quenching can be independently determined through fluorescence lifetime measurements, by monitoring the ZnP fluorescence decays at 605 and 660 nm. Importantly, the fluorescence lifetime experiments allow separation of the contributions of ZnP from those of C_{60}. In all cases, the fluorescence decays were best fit by a single exponential function. For all ZnP−Tri references, a lifetime of 2.1 ns was observed, corresponding to a decay rate of $\sim 5 \times 10^8$ s^{-1}. As shown in Table 4, all six conjugates exhibit fluorescence lifetimes between 0.1 and 0.4 ns, corresponding to decay rates of 2.5×10^9 to 1×10^{10} s^{-1}. The dependence of the fluorescence lifetimes on connectivity pattern and solvent agrees with the results from the steady-state fluorescence experiments.

In summary, both steady-state and time-resolved fluorescence data indicate that a very rapid decay of the ZnP singlet excited state prevails in all six ZnP−Tri−C_{60} conjugates.

4.3. Transient Absorption Spectroscopy. Insight into the nature of the processes following photoexcitation of the ZnP−Tri−C_{60} conjugates **17**−**22** was obtained using femtosecond and nanosecond transient absorption spectroscopy. Photoexcitation of the ZnP−Tri references (**7**, **8**, **9**, **15**, and **16**) at 387 and 355 nm leads to the appearance of spectral features of ZnP singlet excited states. In toluene, the ZnP singlet excited states are characterized by the bleaching of the Q-band absorption at 550 nm and the appearance of broad absorption between 570 and 750 nm. In THF and benzonitrile, the bleaching of the Q-band absorption shifts to 565 nm. The formation of the ZnP singlet excited state ($E_{singlet}$ = 2.00 eV) occurs on the picosecond time scale (1×10^{12} s^{-1}). The ZnP singlet is then deactivated via a slow intersystem crossing process (4.0×10^8 s^{-1}) to the energetically lower-lying triplet excited state ($E_{triplet}$ = 1.53 eV) (Figure S19, Supporting Information). The transient absorption spectra of the ZnP−Tri references revealed a component that rises in ~ 6 ps, which is slightly shorter in the less polar solvents —THF and toluene. This component might be ascribed to an excited state conformational change or intermolecular vibrational cooling by dissipation of excess energy with the solvent.[45]

For the ZnP−Tri−C_{60} conjugates **17**−**22**, the strong ZnP singlet−singlet absorption (570−750 nm) grows in immediately after laser excitation ($k \sim 1 \times 10^{12}$ s^{-1}), indicating the successful formation of the ZnP singlet excited states in the presence

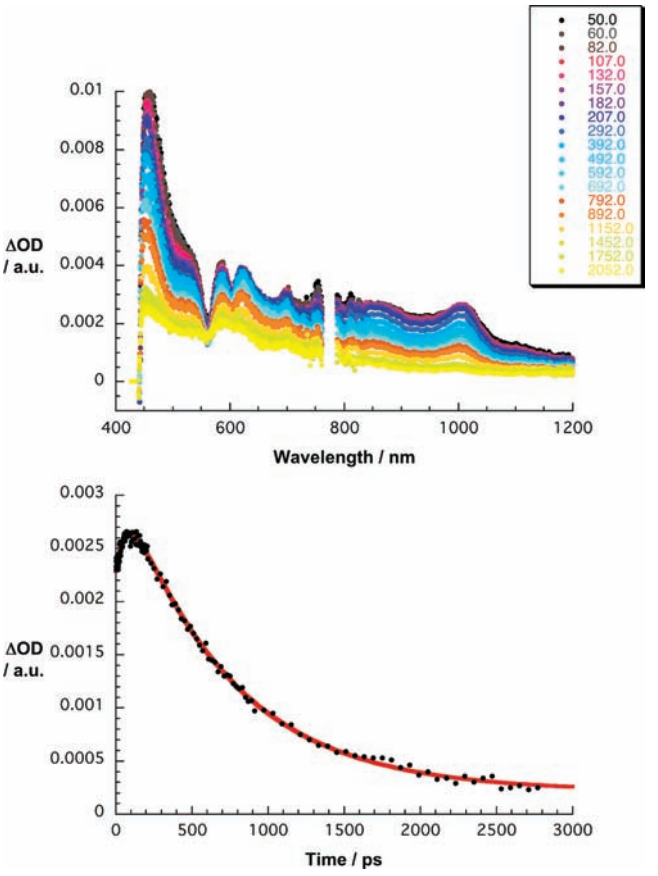

Figure 13. Top: transient absorption spectra (visible and near-infrared) observed upon femtosecond excitation (387 nm, 180 mJ) of *p*1*m*-ZnP−Tri−C_{60} **21** in benzonitrile at room temperature with time delays between 0 and 3000 ps. Bottom: time−absorption profiles of the spectra on the left at 620 nm, monitoring the kinetics of charge separation.

of C_{60}. In these systems, the singlet−singlet absorption decays with accelerated dynamics instead of the slow intersystem crossing dynamics exhibited by the ZnP reference materials. The singlet excited state lifetimes τ_s, determined from an average of first-order fits of the time−absorption profiles at various wavelengths, are listed in Table 4. The values agree well with the lifetimes τ_f derived from the fluorescence decay experiments.

However, the differential absorption spectra observed after completion of the ZnP singlet excited state decay bear no resemblance to those of the ZnP triplet excited state.[46] The new features, which develop simultaneously with ^{1}ZnP* decay, include (1) broad absorption in the 600−700 nm region and (2) absorption in the near-infrared region with a maximum near 1020 nm (see Figures 13 and 14). The first absorption band corresponds to the transient absorption of the one-electron oxidized form of ZnP ($ZnP^{\bullet+}$),[47] and the latter absorption is the signature of the one-electron reduced form of C_{60} ($C_{60}^{\bullet-}$).[48] These results indicate that the charge-separated radical ion-pair (CSRP) state $ZnP^{\bullet+}$−Tri−$C_{60}^{\bullet-}$ is generated from the ZnP singlet excited state in all six ZnP−Tri−C_{60} conjugates. However, owing to the close proximity between ZnP and C_{60} in *m*4*m*-ZnP−Tri−C_{60} **17**, formation of a very short-lived exciplex intermediate cannot be ruled out. Nevertheless, the initial rise in $C_{60}^{\bullet-}$, which is seen in all of the ZnP−Tri−C_{60} conjugates, prompts us to invoke evolution of charge separation from a local excited state.

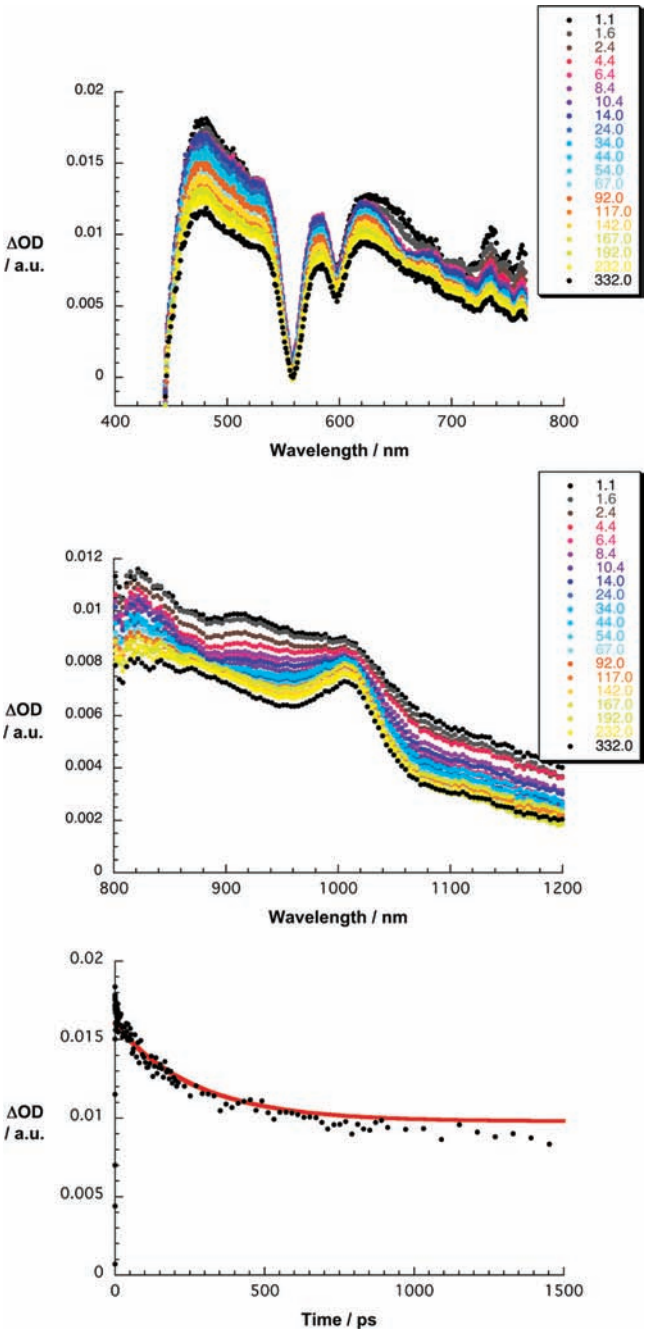

Figure 14. Transient absorption spectra in the visible (top) and near-infrared (middle) regions observed upon femtosecond flash photolysis (387 nm, 150 mJ) of *m*4*p*-ZnP−Tri−C_{60} (**18**) in toluene at room temperature with time delays between 0 and 3000 ps. Bottom: time−absorption profiles of the spectra on the left at 480 nm, monitoring the kinetics of charge separation.

The spectral features of the $ZnP^{\bullet+}$−Tri−$C_{60}^{\bullet-}$ state persist on the picosecond time scale. Determination of the CSRP lifetimes required the use of nanosecond transient absorption spectroscopy. Upon nanosecond flash excitation of the conjugates at 355 nm in oxygenated solutions, it was possible to follow the decay of the $C_{60}^{\bullet-}$ absorption at 1000 nm and that of $ZnP^{\bullet+}$ in the 600−800 nm range (Figure 15).[49] Fitting the decay profiles with single exponential kinetics afforded value for the CSRP lifetimes τ_{csrp} in the submicrosecond time domain

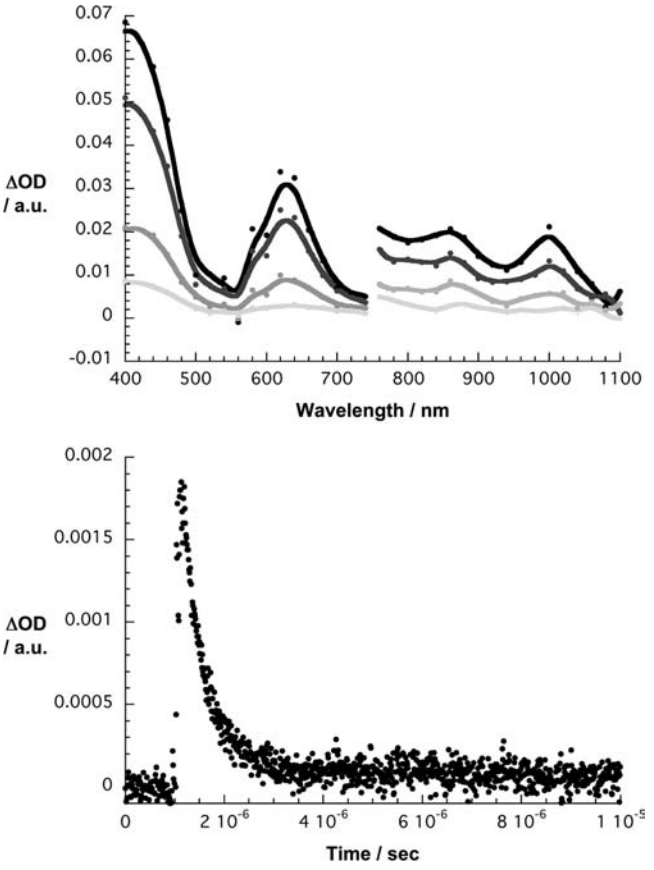

Figure 15. Top: transient absorption spectra (visible and near-infrared) observed upon nanosecond flash photolysis (355 nm) of *p*1*m*-ZnP−Tri−C_{60} **21** in benzonitrile at room temperature with time delays of 250, 400, 800, and 1500 ns. Bottom: time−absorption profiles of the spectra on the left at 1000 nm, monitoring the charge recombination process.

(400−850 ns) as given in Table 4. All ZnP−Tri−C_{60} conjugates, with the significant exception of *m*4*m*-ZnP−Tri−C_{60} (**17**), had shorter CSRP lifetimes in the more polar solvent benzonitrile than in THF. Conjugate *m*4*p*-ZnP−Tri−C_{60} (**18**), for instance, shows CSRP lifetimes of 522 and 440 ns in THF and benzonitrile, respectively. The longest lifetimes were observed for *p*1*p*-ZnP−Tri−C_{60} **20** with values of 844 and 646 ns in benzonitrile and THF, respectively. Remarkably, for **17** there is no difference between the CSRP lifetimes in THF and in benzonitrile, which indicates that through-space ET is occurring due to the close proximity of the ZnP and C_{60} moieties (vide supra). An energy level diagram showing the decay pathways upon excitation of *p*1*p*-ZnP−Tri−C_{60} (**20**) at 425 nm is shown in Figure 16.

The thermodynamic driving force for charge recombination (CR) $-\Delta G^{\circ}_{et}$ decreases as the solvent polarity increases due to stabilization of the CSRP state. Faster CR kinetics in solvents of higher polarity is indicative of inverted Marcus behavior, i.e., to a process occurring in the region of the Marcus parabola where the ET rates decrease as the values of $-\Delta G^{\circ}_{et}$ increase.[7] In this context, there are three major parameters that govern the ET kinetics at a given temperature: the Gibbs free energy for the ET process (ΔG°_{et}), the reorganization energy λ, and the electronic coupling parameter V. For the present conjugates, ΔG°_{et} can be determined from the relative energies of the ZnP singlet excited state and of the CSRP state. The ZnP singlet excited state energy,

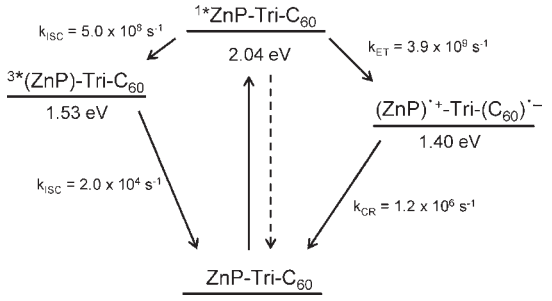

Figure 16. Energy level diagram, proposed decay pathways, and rate constants in s^{-1} for *p*1*p*-ZnP−Tri−C_{60} **20** following excitation at the Soret band in THF. Energy values are derived from transient absorption and electrochemical experiments. k_{ET} = rate constant for electron transfer; k_{CR} = rate constant for charge recombination; and k_{ISC} = rate constant for intersystem crossing.

derived from the crossing of the absorption and emission spectra, is 2.05 eV.[46] The energy of the CSRP state can be derived from the theoretical calculations, namely, the HOMO−LUMO gaps (1.5 eV), or from electrochemical measurements (1.4 eV), as the difference between the first ZnP oxidation potential and the first C_{60} reduction potential, with solvent correction, according to the Weller equation.[50] The reorganization energies λ are assumed to be the same for all six ZnP−Tri−C_{60} conjugates since, with the exception of *m*4*m*-ZnP−Tri−C_{60} (**17**), similar lowest energy conformations for these isomeric conjugates were found by theoretical calculations. These considerations leave the electronic coupling as the only variable in evaluating changes in the CR and CS dynamics. To determine the subtle influence of the connectivity pattern on electronic coupling between ZnP and C_{60}, the detailed theoretical analysis described earlier was undertaken.

For conjugates with *para*-connectivity, the dependence of fluorescence quantum yields and lifetimes of the CSRP states on the solvent polarity is consistent with a through-bond ET mechanism. However, for conjugates with *meta*-connectivity, the solvent dependence is weaker and becomes negligible in the case of **17**. The shorter donor−acceptor separation in *meta*-linked conjugates may induce additional through-space coupling.

Considering the linkage of ZnP to either the C or N atom of the triazole, an increase of the charge separation rate is observed when the electron-donating ZnP is linked to the carbon atom of the triazole ring rather than to nitrogen. This result is in agreement with the theoretical analysis, where it was found that linking the ZnP to the carbon atoms lowers the HOMO/LUMO gap and therefore facilitates charge injection into the bridge. It also explains the accelerated charge separation dynamics. Note that the effective center-to-center distances in these conjugates are nearly constant, 19.4 vs 19.1 Å for *p*4*p*-ZnP−Tri−C_{60} (**19**) and *p*1*p*-ZnP−Tri−C_{60} (**20**) and 15.3 vs 16.7 Å for *p*4*m*-ZnP−Tri−C_{60} (**22**) and *p*1*m*-ZnP−Tri−C_{60} (**21**), respectively. Moreover, a decrease in the charge recombination rate can be observed when the electron-donating ZnP is linked to the nitrogen atom of the triazole ring rather than to the triazole carbon, namely, 1.8×10^{-6} vs 1.5×10^{-6} s^{-1} for *p*4*p* **19** and *p*1*p* **20** and 2.5×10^{-6} vs 2.1×10^{-6} s^{-1} for *p*4*m* **22** and *p*1*m* **21** in benzonitrile, respectively. The calculated EA values on the triazole rings for each conjugate correlate well with the CR dynamics. Only the behavior of conjugate **18** deviates from the theoretical trend, as its k_{cr} value is comparable to that of *p*4*m* conjugate **22**, despite its higher EA value.

Comparison between the *para* vs *meta* substitution pattern on the triazole-linked phenyl rings shows that higher electron affinity (EA) values (see above) are found in the case of *meta* substitution on both sides of the triazole ring, suggesting that the ET process is facilitated in *meta*-linked conjugates due to available lower-energy states. Focusing on the CR process, the k_{cr} values of the conjugates are larger for *meta* than *para* connectivity, namely, 2.1×10^{-6} vs 1.5×10^{-6} s^{-1} for *p*1*m*-ZnP−Tri−C_{60} (**21**) and *p*1*p*-ZnP−Tri−C_{60} (**20**) and 2.5×10^{-6} vs 1.8×10^{-6} s^{-1} for *p*4*m*-ZnP−Tri−C_{60} (**22**) and *p*4*p*-ZnP−Tri−C_{60} (**19**) in benzonitrile, respectively. Thus, incorporating *meta* connectivity accelerates the charge recombination process. This effect is similar to the changes that are imposed by the variation in the ZnP linkage to the triazole, i.e., whether it is connected via a nitrogen or carbon atom.

The variation of connectivity at the triazole moieties significantly affects the electronic properties of the conjugates, as reflected by the electron affinity calculations. Thus, we propose that the values of EA at the triazole linker strongly affect electronic coupling among the six ZnP−Tri−C_{60} conjugates; i.e., the higher the EA value, the stronger the coupling. On this basis, we conclude that the scale of electronic coupling in the conjugates is as follows: *p*1*p*-ZnP−Tri−C_{60} (**20**) < *p*1*m*-ZnP−Tri−C_{60} (**21**) ≤ *p*4*p*-ZnP−Tri−C_{60} (**19**) < *p*4*m*-ZnP−Tri−C_{60} (**22**).

CONCLUSIONS

A series of ZnP−Tri−C_{60} conjugates have been synthesized using "click chemistry" from electron donor and acceptor fragments containing terminal alkyne and azide functionality. The photophysical properties of these conjugates clearly demonstrate that 1,2,3-triazoles represent excellent bridges for rapid and efficient photoinduced electron transfer (ET) between remote electron donor and acceptor moieties, in the present case ZnP and C_{60}, respectively. The photophysics of the ZnP−Tri−C_{60} conjugates also reflect a significant influence of the substitution pattern of the bridge, most prominently with respect to the dynamics of charge recombination. Except for *m*4*m*-ZnP−Tri−C_{60} (**17**), all the conjugates undergo through-bond ET processes, for both charge separation and charge recombination. For **17**, the proximity of the ZnP and C_{60} moieties allows for the occurrence of through-space ET processes. The long lifetimes of the charge-separated radical ion-pair (CSRP) states of these conjugated materials, in the range of 415−850 ns, in THF and benzonitrile, show that charge recombination occurs in the Marcus inverted region.[3−7,9] Similar submicrosecond CSRP lifetimes have been observed for other types of covalently linked ZnP−C_{60} hybrids studied by us, with polyether, alkyne, and azo linkers.[10b,10c,43] Since the through-bond distance is nearly equal in all the conjugates, the variation in charge separation and charge recombination dynamics in the ZnP−Tri−C_{60} conjugates must be ascribed to changes in the electronic properties of these materials, including orbital energies, electron affinity, and the energies of the excited states. The changes in the electronic couplings are, in turn, a consequence of the different connectivity patterns at the 1,4-diphenyl-1,2,3-triazole linker.

EXPERIMENTAL SECTION

1. General Information and Materials. NMR spectra were obtained on either a Bruker AVANCE 400 (400 MHz) or AVANCE 800 (800 MHz) spectrometer using $CDCl_3$ solvents as the lock. The spectra were collected at 25 °C, and chemical shifts (δ, ppm) were referenced to the tetramethylsilane internal standard (0.1% v/v). In the assignments, the chemical shift (in ppm) is given first, followed, in brackets, by multiplicity (s, singlet; d, doublet; t, triplet; m, multiplet; br, broad), the value of the coupling constants in Hz if applicable, the number of protons implied, and finally the assignment. Mass spectra were obtained on an Agilent 1100 Series Capillary LCMSD Trap XCT spectrometer in positive- or negative-ion mode and a Thermo-Finnigan PolarisQ ion-trap GCMS spectrometer. MALDI-TOF mass spectra were recorded in a Bruker OmniFLEX MALDI-TOF MS spectrometer. This instrument was operated at an accelerating potential of 20 kV in linear mode. The mass spectra represent an average over 256 consecutive laser shots. The mass scale was calibrated using the matrix peaks and the calibration software available from Bruker OmniFLEX. Values of m/z correspond to monoisotopic masses. MALDI-TOF mass spectra were obtained without using a matrix unless otherwise noted. MALDI-TOF mass calibrations were performed using tetra[3,5-di(*tert*-butyl)phenyl]porphyrin and pristine C_{60}. All chemicals were purchased from Sigma-Aldrich and used without further purification. The progress of the reactions was monitored by thin-layer chromatography (TLC) whenever possible. TLC was performed using precoated glass plates (Silica gel 60, 0.25 mm thickness) containing a 254 nm fluorescent indicator. Column chromatography was carried out using Merck Silica gel 60 (0.063−0.200 mm) and neutral alumina (Brockmann I, activated, 150 mesh, 58 Å). Infrared spectra were obtained using a Thermo Nicolet Avatar 360 FTIR spectrophotometer.

2. Electrochemical Studies. The samples were all analyzed in oxygen-free anhydrous dichloromethane (DCM). Tetrabutylammonium hexafluorophosphate ($TBAPF_6$) was added as supporting electrolyte. $TBAPF_6$ was recrystallized two times from ethanol and dried under vacuum for 24 h prior to use. Cyclic voltammetry (CV) and differential pulse voltammetry (DPV) were performed with a CH Instruments potentiostat under an argon atmosphere at room temperature at a scan rate of 100 mV s^{-1} and pulse rate of 0.05 s with increments of 4 mV and an amplitude of 50 mV. A standard three-electrode setup was used, consisting of a glassy carbon working electrode (Cypress, 1.0 mm), a platinum wire auxiliary electrode (Aldrich, 1.0 mm), and a nonaqueous silver/silver nitrate ($Ag/AgNO_3$) reference electrode (calibrated externally versus the ferrocene/ferrocenium (Fc/Fc+) redox couple). The half-wave potential, $E_{1/2}$, was determined as $(E_{pa} + E_{pc})/2$, where E_{pa} and E_{pc} are the anodic and cathodic peak potentials from the CV. Additionally, $E_{1/2}$ was corroborated by DPV experiments using the equation: $E_{max(DPV)} = E_{1/2} - (\Delta E/2)$, where ΔE is the pulse amplitude (50 mV).

3. Photophysical Studies. All solvents used were spectroscopic grade (99.5%) and were purchased from Sigma-Aldrich. Femtosecond transient absorption studies were performed with 387 and 420 nm laser pulses (1 kHz, 150 fs pulse width) from an amplified Ti:Sapphire laser system (model CPA 2101, Clark-MXR Inc.). Nanosecond Laser Flash Photolysis experiments were performed with 355 or 532 nm laser pulses from a Quanta-Ray CDR Nd:YAG system (6 ns pulse width) in a front face excitation geometry. Fluorescence lifetimes were measured using a Fluorolog (Horiba Jobin Yvon). Steady-state fluorescence measurement were performed using a Fluoromax 3 (Horiba Jobin Yvon). The experiments were performed at room temperature.

4. Synthesis. *Synthesis of 3-(Trimethylsilyl)ethynylbenzaldehyde (**1**).* Bis(benzonitrile)palladium(II) chloride (0.325 mmol,

130 mg) and copper(I) iodide (0.216 mmol, 42 mg) were added to a flask which was then sparged with argon and charged with dioxane (11 mL). In a separate flask, tri-*tert*-butylphosphine (0.60 g) was added to dioxane (11 mL) to create a 0.27 M solution. A 2.2 mL aliquot of this solution was added to the flask containing the palladium and copper catalysts, turning the solution dark. Diisopropylamine (13 mmol, 1.8 mL), 3-bromobenzaldehyde (10.8 mmol, 1.26 mL), and trimethylsilylacetylene (13 mmol, 1.8 mL) were all added to the reaction flask by syringe. After ~30 min the solution bacame warm, and a precipitate formed, turning the reaction mixture nearly solid. The reaction was run for 7 h before being diluted with ethyl acetate and filtered through a short silica funnel. The product was purified on a silica column using a 1:1 mixture of hexanes and methylene chloride as the eluent to afford a yellow oil in quantitative yield. ^{1}H NMR (400 MHz, $CDCl_3$): δ =10.0 ppm (s, 1H, CHO), 7.9 ppm (s, 1H, ArH), 7.8 ppm (d, 1H, ArH), 7.7 ppm (d, 1H, ArH), 7.5 ppm (t, 1H, ArH), 0.3 ppm (s, 9H, TMS).

*Synthesis of Zinc(II)-5-(3-ethynylphenyl)-10,15,20-tris-(3,5-di-tert-butylphenyl) Porphyrin (m-ZnP) (**3**) and Zinc(II)-5-(4-ethynylphenyl)-10,15,20-tris-(3,5-di-tert-butylphenyl) Porphyrin (p-ZnP) (**4**).* Tetraphenylphosphonium chloride (0.19 mmol, 71 mg), 3-TMS-ethynylbenzaldehyde (**1**), or 4-TMS-ethynylbenzaldehyde (**2**) (15.3 mmol, 3.08 g) and 3,5-di-*tert*-butylbenzaldehyde (45.8 mmol, 10 g) were dissolved in a flask containing dichloromethane (600 mL). The flask was sealed and purged with argon. Freshly distilled pyrrole (61.1 mmol, 4.2 mL) and boron trifluoride diethyl etherate (6 mmol, 1 mL of 1 M solution in CH_2Cl_2 made from 8.1 M stock solution) were added by syringe. The reaction flask was protected from light using aluminum foil and stirred at room temperature for 1 h. The resulting porphyrinogen was oxidized by adding 2,3-dichloro-5,6-dicyano-*p*-benzoquinone (DDQ) (45.9 mmol, 10.56 g) and stirring overnight. Triethylamine (6 mmol, 0.84 mL) was added to neutralize the solution which was then filtered through a pad of silica using CH_2Cl_2 as eluent. The solution was concentrated, and the porphyrin was then metalated by adding an excess of $Zn(OAc)_2 \cdot 2H_2O$ (3.5 g) in MeOH (35 mL) and heating at reflux for 1 h. Solvent was evaporated and the product dissolved in $CHCl_3$/THF (1:1, 250 mL). Tetrabutylammonium fluoride (TBAF) (1.0 M solution in THF, 90 mL) was added, and the solution was stirred at rt for 1 h. Glacial acetic acid (25 mL) was added, and the product was washed over a silica funnel with $CHCl_3$. Yield was ~5 g (31%).

*m-ZnP (**3**).* Purified by column chromatography (silica gel, CH_2Cl_2). ^{1}H NMR (400 MHz, $CDCl_3$): δ = 9.0 ppm (q, 6H, βH), 8.9 ppm (t, 2H, βH), 8.4 ppm (s, 1H, ArH), 8.2 ppm (d, 1H, ArH), 8.0 ppm (m, 6H, 3,5-di-*tert*-Bu-Ar-meta-H), 7.9 ppm (d, 1H, ArH), 7.8 ppm (m, 3H, 3,5-di-*tert*-Bu-Ar-para-H), 7.7 ppm (t, 1H, ArH), 3.1 ppm (s, 1H, alkynyl-H), 1.5 (s, 54H, *tert*-BuH). MALDI-TOF calculated for $C_{70}H_{76}N_4Zn$ = 1036.54 [M^+], found 1036.2 [M^+].

*p-ZnP (**4**).* Purified by column chromatography (neutral alumina, CH_2Cl_2/hexanes, 1:9). ^{1}H NMR (400 MHz, $CDCl_3$): δ = 9.0 ppm (d, 6H, βH), 8.9 ppm (d, 2H, βH), 8.2 ppm (d, 2H, ArH), 8.0 ppm (s, 6H, 3,5-di-*tert*-Bu-Ar-meta-H), 7.9 ppm (d, 2H, ArH), 7.8 ppm (s, 3H, 3,5-di-*tert*-Bu-Ar-para-H), 3.3 ppm (s, 1H, alkyne-H), 1.5 ppm (s, 54H, *tert*-BuH). MALDI-TOF calculated for $C_{70}H_{76}N_4Zn$ = 1036.54 [M^+], found 1036.9 [M^+].

*General Procedure for Synthesis of Azidobenzaldehydes (**5**, **6**).* Bromobenzaldehyde (1 g, 5.4 mmol), sodium azide (0.7 g, 10.8 mmol), sodium ascorbate (53 mg, 0.27 mmol), copper(I) iodide (0.1 g, 0.54 mmol), and EtOH/H_2O (10 mL, 7:3 ratio) were added to a flask which was then degassed with argon for 10 min. *N*,*N*′-Dimethylethylenediamine (0.9 mL, 0.81 mmol) was added to the flask, and the solution turned blue. The reaction was heated at reflux for 1.5 h and monitored by FTIR for the appearance of the azide band near 2100 cm^{-1}. After cooling to rt, water was added to the solution which was then extracted with 50 mL of methylene chloride. The product was purified on a silica column using methylene chloride. Some unreacted starting material remained which could not be easily separated due to similar R_f. The presence of residual bromobenzaldehyde was not a problem because it does not react in the following reaction to form triazoles and can be separated afterward. The ratios of product to starting material were obtained by ^{1}H NMR and used in calculations of quantities of reagents needed for the triazole reaction.

NOTE. In retrospect, the use of *N*,*N*′-dimethylethylenediamine as a catalyst in this case is problematic, as it can form an imine with the aldehyde, which was actually observed in later studies. Hydrolysis after the reaction would increase the final product yield. No aldehydes were tested with respect to imine formation in the cited reference 28.

*3-Azidobenzaldehyde (**5**).* 88% purity by ^{1}H NMR. 30% overall yield. ^{1}H NMR (400 MHz, $CDCl_3$): 10.0 ppm (s, 1H, CHO), 7.6 ppm (d, 1H, ArH), 7.5 ppm (m, 2H, ArH), 7.2 ppm (d, 1H, ArH).

*4-Azidobenzaldehyde (**6**).* 37% purity by ^{1}H NMR. 30% overall yield. ^{1}H NMR (400 MHz, $CDCl_3$): 9.95 ppm (s, 1H, CHO), 7.9 ppm (d, 2H, ArH), 7.15 ppm (d, 2H, ArH). Note: the spectrum shows peaks for CH_2Cl_2 (5.3 ppm), acetone (2.1 ppm), and toluene (2.3 ppm, 7.1 ppm, 7.2 ppm).

*General Procedure for Synthesis of Zinc Porphyrin Triazoles (**7**, **8**, **9**).* In a small round-bottomed flask were added alkynyl-porphyrin (**3** or **4**, 813 mg, 0.78 mmol), azidobenzaldehyde (**5** or **6**, 115 mg, 0.78 mmol), copper(I) iodide (15 mg, 78 μmol), and sodium ascorbate (31 mg, 0.16 mmol). A 9:1 mixture of DMSO/H_2O (30 mL) was added, and the flask was purged with argon. The reactions were run in a CEM Discover LabMate microwave reactor at a power setting of 50 W for 30 min. The reaction was cooled constantly during the reaction with a stream of air blown into the reaction chamber to maintain a temperature of 80 ^oC. Microwave power adjusts automatically to help maintain the set reaction temperature. The product was extracted using CH_2Cl_2 and purified by column chromatography (silica gel, CH_2Cl_2). The starting *m*-alkynyl-porphyrin was not pure but was a mixture of the alkynyl porphyrin and the tetra-(3,5-di-*tert*-butylphenyl) porphyrin that is a byproduct of its synthesis. Since the tetraaryl porphyrin does not react in this step, it is easily separated out during chromatography. Yields of *m*4*m*-ZnP−Tri and *m*4*p*-ZnP−Tri were calculated from the estimated 50% of *m*-alkynyl−porphyrin in the mixture of starting porphyrin.

m,4,*m*-ZnP−Triazole−Benzaldehyde (*m*4*m*-ZnP−Tri) (**7**) was obtained in 28.7% yield. ^{1}H NMR (400 MHz, $CDCl_3$): δ = 10.0 ppm (s, 1H, CHO), 9.0 ppm (m, 8H, βH), 8.7 ppm (s, 1H, ArH), 8.4 ppm (d, 1H, ArH), 8.35 ppm (s, 1H, triazole-H), 8.3 ppm (d, 1H, ArH), 8.15 ppm (s, 1H, CHO-Ar**H**), 8.1−8.0 ppm (m, 6H, 3,5-di-*tert*-Bu-Ar-meta-H), 8.0 ppm (d, 1H, CHO-Ar**H**), 7.9 ppm (t, 1H, ArH), 7.8 ppm (m, 4H, 3,5-di-*tert*-Bu-Ar-para-H and CHO-Ar**H**), 7.6 ppm (t, 1H, CHO-Ar**H**), 1.5 ppm (s, 54H, *tert*-BuH). MALDI-TOF calculated for $C_{77}H_{81}N_7OZn$ = 1183.58 [M^+], 1155.57 [M − 28]. Found: 1183.6 [M^+], 1155.1 [M − 28].

m,4,*p*-ZnP−Triazole−Benzaldehyde (*m*4*p*-ZnP−Tri) (**8**) was obtained in quantitative yield. ^{1}H NMR (400 MHz, $CDCl_3$): δ = 9.9 ppm (s, 1H, CHO), 9.0 ppm (m, 8H, βH), 8.7 ppm (s, 1H, ArH), 8.4 ppm (d, 1H, ArH), 8.35 ppm (s, 1H, triazole-H), 8.3 ppm (d, 1H, ArH), 8.2 ppm (m, 6H, 3,5-di-*tert*-Bu-Ar-meta-H), 7.9 ppm (m, 5H, ArH and CHO-Ar**H**), 7.8 ppm (s, 3H, 3,5-di-*tert*-Bu-Ar-para-H), 1.5 ppm (s, 54H, *tert*-BuH). MALDI-TOF calculated for $C_{77}H_{81}N_7OZn$ = 1183.58 [M^+], 1155.57 [M − 28] for loss of nitrogen from the triazole ring. Found: 1183.6 [M^+], 1155.5 [M − 28].

p,4,*p*-ZnP-Triazole−benzaldehyde (*p*4*p*-ZnP−Tri) (**9**) was obtained in 40% yield. ^{1}H NMR (400 MHz, $CDCl_3$): δ = 10.1 ppm (s, 1H, CHO), 9.0 ppm (m, 8H, βH), 8.5 ppm (s, 1H, triazole-H), 8.4 ppm (d, 2H, ArH), 8.3 ppm (d, 2H, ArH), 8.14 ppm (s, 4H, CHO-Ar**H**), 8.1 ppm (m, 6H, 3,5-di-*tert*-Bu-Ar-meta-H), 7.8 ppm (m, 3H, 3,5-di-*tert*-Bu-Ar-para-H), 1.5 ppm (s, 54H, *tert*-BuH). MALDI-TOF calculated for $C_{77}H_{81}N_7OZn$ = 1183.58 [M^+], 1155.57 [M − 28] for loss of nitrogen from the triazole ring. Found: 1182.6 [M^+], 1154.8 [M − 28].

*Synthesis of 5-(4-Acetamidophenyl)-10,15,20-tris-(3,5-di-tert-butylphenyl) Porphyrin (**10**).* 3,5-Di-*tert*-butylbenzaldehyde (1.637 g, 7.5 mmol) and *p*-acetamidobenzaldehyde (0.410 g, 2.5 mmol) were dissolved in 1 L of CH_2Cl_2 contained in a 2 L three-neck flask. The flask was covered with aluminum foil and purged with N_2 for 10 min before freshly distilled pyrrole (700 μL, 10 mmol) was injected. The reaction was stirred for another 10 min, and the reaction was initiated by the injection of TFA (1.4 mL, 20 mmol). After the reaction was stirred at room temperature for 1.5 h, DDQ (1.70 g, 7.5 mmol) was added, and the reaction was stirred for 1 h at room temperature and was then neutralized with triethylamine (2.8 mL, 20 mmol). The crude mixture was purified with silica gel flash chromatography; elution with CH_2Cl_2 removed all tetrarylporphyrin, and the desired A_3B porphyrin was then eluted with 20% EtOAc in CH_2Cl_2. Solvent was removed under vacuum, affording a purple solid in a yield of ∼18%. ^{1}H NMR (400 MHz, $CDCl_3$): δ = 8.8 ppm (s, 4H, βH), 8.8 ppm (d, 2H, βH), 8.7 ppm (d, 2H, βH), 8.0 ppm (m, 6H, Ar-meta-H), 7.9 ppm (d, 2H, ArH), 7.7 ppm (m, 3H, Ar-para-H), 7.4 ppm (d, 2H, ArH), 7.1 ppm (s, 1H, NH), 2.0 ppm (s, 3H, CH_3), 1.4 ppm (s, 54H, *tert*-BuH), −2.8 ppm (s, 2H, pyrrole H). MALDI-TOF calculated for $C_{70}H_{80}N_5O$ = 1006.64 [M^+]. Found: 1007.43 [M^+].

*Synthesis of 5-(4-Aminophenyl)-10,15,20-tris-(3,5-di-tert-butylphenyl) Porphyrin (**11**).* *p*-Amidophenyltriarylporphyrin (**10**) (0.2067 g, 0.2 mmol) was dissolved in 60 mL of EtOH in a 250 mL flask. Concentrated HCl (40 mL) was added to the reaction mixture, which was heated at reflux for 17 h. The crude mixture was diluted with water and extracted with CH_2Cl_2 five times. The organic layer was washed with H_2O three times and with saturated $NaHCO_3$ solution twice. The pooled organic layer was dried over Na_2SO_4 and filtered. The solvent was removed under vacuum, and flash chromatography with silica gel and CH_2Cl_2 afforded the desired aminophenylporphyrin in quantitative yield. ^{1}H NMR (400 MHz, $CDCl_3$): δ = 8.8 ppm (d, 2H, βH), 8.8 ppm (m, 6H, βH), 8.0 ppm (m, 6H, Ar-meta-H), 7.9 ppm (d, 2H, ArH), 7.7 ppm (m, 3H, Ar-para-H), 6.9 ppm (d, 2H, ArH), 3.9 ppm (s, 2H, NH_2), 1.4 ppm (d, 54H, *tert*-BuH), −2.7 ppm (s, 2H, pyrrole H). MALDI-TOF calculated for $C_{68}H_{79}N_5$ = 965.63 [M^+]. Found: 966.64 [M^+].

*Synthesis of Zinc(II)-5-(4-azidophenyl)-10,15,20-tris-(3,5-di-tert-butylphenyl) Porphyrin (**12**).* *p*-Aminophenyltriarylporphyrin (**11**) (0.1896 g, 0.1961 mmol) was dissolved in 3.17 mL of TFA in a 10 mL flask and cooled to 0 °C in an ice bath. Sodium nitrite (0.0271 g, 0.3922 mmol) was dissolved in 0.75 mL of distilled water and added to the reaction, which was then stirred for 15 min at 0 °C. Sodium azide (0.0382 g, 0.5883 mmol) was dissolved in 0.75 mL of distilled water and added to the reaction mixture. After the reaction was stirred on ice for 1 h, cold water was added to the flask. The crude mixture was extracted with CH_2Cl_2, and the green organic layer was washed with water until it turned purple. The organic phase was dried over $MgSO_4$, filtered, and concentrated under vacuum to about 150 mL. Zinc acetate (0.50 g, 2.28 mmol) was dissolved in ∼15 mL of MeOH and added to the porphyrin solution. The reaction was heated at reflux for 1 h, and the crude mixture was washed with water three times. The organic layer was dried over $MgSO_4$ and filtered. Flash column chromatography with silica gel was used to purify the crude material using 2:1 CH_2Cl_2:hexanes as the eluent, and the desired product was eluted with the solvent front. The yield for this two-step reaction was ∼62%. ^{1}H NMR (400 MHz, $CDCl_3$): δ = 8.9 ppm (m, 6H, βH), 8.8 ppm (d, 2H, βH), 8.1 ppm (d, 2H, ArH), 8.0 ppm (s, 6H, Ar-meta-H), 7.7 ppm (s, 3H, Ar-para-H), 7.1 ppm (d, 2H, ArH), 1.4 ppm (s, 54H, *tert*-BuH). MALDI-TOF calculated for $C_{68}H_{75}N_7Zn$ = 1053.54 [M^+], 1025.54 [M − 28]. Found: 1027.43 [M − 28] and 2056.85 [2 (M − 28)]. IR: a strong azide peak was seen at 2120 cm^{-1}.

NOTE. The mass at 2056.85 is attributed to dimerization of the porphyrin in the MALDI instrument. When light from the laser hits the azide, N_2 is lost yielding a very reactive aryl nitrene. Two aryl nitrenes then come together to form the dimer. There is also a visible color change of this porphyrin from purple to green in solution upon exposure to light.

*Synthesis of p-Ethynylbenzaldehyde (**13**).* *p*-(Trimethylsilyl)-ethynylbenzaldehyde (0.202 g, 1 mmol) and K_2CO_3 (0.014 g, 0.1 mmol) were dissolved in 11.7 mL of MeOH. The reaction was stirred at room temperature for 3 h, and the solvent was removed under vacuum. The solid was redissolved in CH_2Cl_2 and washed with aqueous $NaHCO_3$ three times. The organic layer was dried over Na_2SO_4 and afforded a yellow solid in ∼96% yield after solvent was removed. ^{1}H NMR (400 MHz, $CDCl_3$): δ = 9.9 ppm (s, 1H, CHO), 7.7 ppm (d, 2H, ArH), 7.5 ppm (d, 2H, ArH), 3.2 ppm (s, 1H, ethynyl H).

*Synthesis of m-Ethynylbenzaldehyde (**14**).* *m*-(Trimethylsilyl)-ethynylbenzaldehyde (0.340 g, 1.68 mmol) was dissolved in 50 mL of methylene chloride in a flask containing a stir bar. Tetrabutylammonium fluoride (3.36 mL, 1.0 M in THF, 3.36 mmol) was added to the reaction mixture, which was stirred at room temperature for 5 min. Flash silica gel chromatography with CH_2Cl_2 as an eluent was used to purify the crude mixture. Fractions were collected, and the progress of separation was monitored by TLC. Solvent was removed under vacuum and afforded a yellow solid in ∼65%. ^{1}H NMR (400 MHz, $CDCl_3$): δ = 10.0 ppm (s, 1H, CHO), 8.0 ppm (s, 1H, ArH), 7.9 ppm (d, 1H, ArH), 7.7 ppm (d, 1H, ArH), 7.5 ppm (t, 1H, ArH), 3.2 ppm (s, 1H, ethynyl H).

*Synthesis of p,1,p-ZnP-Triazole−Benzaldehyde (**15**).* *p*-Azidophenyltriarylzinc(II)porphyrin (**12**) (0.0500 g, 0.0474 mmol), *p*-ethynylbenzaldehyde (**13**) (0.0185 g, 0.1421 mmol), copper(I) iodide (0.0028 g, 0.0142 mmol), sodium ascorbate (0.0056 g, 0.0284 mmol), and TBTA (0.0075 g, 0.0142 mmol) were suspended and sonicated in 1.78 mL of DMSO in a 10 mL microwave reaction vessel. Distilled water (0.2 mL) was added to the mixture, and the reaction vessel was capped with a Teflon septum. The reaction mixture was stirred vigorously and purged with N_2 for 5 min before the vessel was placed into the

microwave reactor. The reaction was run at 50 W microwave power and maintained at 80 °C for 45 min. The reaction mixture was then sonicated and irradiated with microwave for another 15 min under the same power and temperature settings, and this step was repeated until the total reaction time reached 2 h. The reaction progress was monitored by TLC. The crude mixture was first diluted with CH_2Cl_2 and washed twice with aqueous NH_4OH and twice with water. The aqueous layer was extracted with CH_2Cl_2 four times, and the pooled organic layer was washed with water until it turned purple. The organic layer was dried over $MgSO_4$ and filtered, and the solvent was removed under vacuum. Flash column chromatography with silica gel was used to purify the crude product, and eluting the column with 100% CH_2Cl_2 and then with 3% ethyl acetate in CH_2Cl_2 affords the desired porphyrin-triazole-benzaldehyde in ~84% yield. ^{1}H NMR (400 MHz, $CDCl_3$): δ = 10.0 ppm (s, 1H, CHO), 9.0 ppm (m, 6H, βH), 8.9 ppm (d, 2H, βH), 8.5 ppm (s, 1H, triazole-H), 8.4 ppm (d, 2H, ArH), 8.1 ppm (d, 4H, CHO-ArH), 8.0 ppm (m, 6H, 3,5-di-*tert*-Bu-Ar-meta-H), 7.9 ppm (d, 2H, ArH), 7.7 ppm (m, 3H, 3,5-di-*tert*-Bu-Ar-para-H), 1.4 ppm (d, 54H, *tert*-BuH). MALDI-TOF mass calculated $C_{77}H_{81}N_7OZn$ = 1183.58 [M^+], 1155.58 [M − 28]. Found: 1156.29 [M − 28].

*Synthesis of p,1,m-ZnP−Triazole−Benzaldehyde (**16**).* Zn *p*-Azidophenyl (**12**) (0.060 g, 0.0568 mmol), *m*-ethynylbenzaldehyde (**14**) (0.022 g, 0.170 mmol), copper(I) iodide (0.0033 g, 0.0170 mmol), sodium ascorbate (0.0068 g, 0.0341 mmol), and TBTA (0.0091 g, 0.0170 mmol) were suspended and sonicated in 2.0 mL of DMSO in a 10 mL microwave reaction vessel. Distilled water (0.2 mL) was added to the mixture, and the reaction vessel was capped with a Teflon septum. The reaction mixture was purged with N_2 for 5 min before the vessel was placed into the microwave reactor. The reaction was run at 50 W microwave power and maintained at 80 °C for 2 h. During this 2 h reaction, the vessel was removed from the reactor, and the reaction mixture was sonicated for 5 min. The crude mixture was first diluted with CH_2Cl_2 and washed with aqueous NH_4OH twice and with water twice. The aqueous layer was extracted with CH_2Cl_2 four times, and the pooled organic layer was washed with water until it turned purple. The organic layer was dried over $MgSO_4$ and filtered, and the solvent was removed under vacuum. Flash column chromatography with silica gel was used to purify the crude product, and eluting the column with 100% CH_2Cl_2 and then with 3% ethyl acetate in CH_2Cl_2 affords the desired porphyrin-triazole-benzaldehyde in a ~77% yield. ^{1}H NMR (400 MHz, $CDCl_3$): δ = 10.1 ppm (s, 1H, CHO), 9.0 ppm (m, 8H, βH), 8.6 ppm (s, 1H, triazole-H), 8.5 ppm (s, 1H, CHO-Ar**H**), 8.5 ppm (d, 2H, ArH), 8.4 ppm (d, 1H, CHO-Ar**H**), 8.2 ppm (d, 2H, ArH), 8.1 ppm (m, 6H, 3,5-di-*tert*-Bu-Ar-meta-H), 7.9 ppm (d, 1H, CHO-Ar**H**), 7.8 ppm (m, 3H, 3,5-di-*tert*-Bu-Ar-para-H), 7.7 ppm (t, 1H, CHO-Ar**H**), 1.5 ppm (d, 54H, *tert*-BuH). MALDI-TOF mass calculated $C_{77}H_{81}N_7OZn$ = 1183.58 [M^+], 1155.58 [M − 28]. Found: 1156.37 [M − 28].

*Synthesis of Porphyrin−Triazole−Fullerenes (**17**−**21**).* Method 1: porphyrin-triazole-benzaldehyde (12.8 mg, 0.0107 mmol), C_{60} (3.6 mg, 0.005 mmol), and sarcosine (0.9 mg, 0.01 mmol) were dissolved in toluene (2 mL) and heated at reflux overnight. The product was purified by column chromatography (silica gel, hexanes/ethyl acetate 2:1).

Method 2: porphyrin-triazole-benzaldehyde (12.8 mg, 0.0107 mmol), C_{60} (16 mg, 0.022 mmol), and sarcosine (2 mg, 0.022 mmol) were dissolved in toluene (10 mL) and heated at reflux overnight. The product was purified by column chromatography (silica gel, toluene/ethyl acetate 99:1)

m4m-ZnP−Triazole−C_{60} (**17**) was obtained in ~30% yield by method 1 and ~70% yield by method 2. ^{1}H NMR (400 MHz, $CDCl_3$): δ = 8.8−9.0 ppm (m, 8H, H_a), 8.5 ppm (d, 1H, H_b), 8.3 ppm (d, 1H, H_c), 8.1−8.2 ppm (m, 6H, H_d), 8.0 ppm (s, 1H, H_e), 7.83−7.9 ppm (m, 4H, H_f), 7.8 ppm (m, 3H, H_g), 7.7 ppm (d, 1H, H_h), 7.4 ppm (t, 1H, H_i), 4.7 ppm (s, 1H, H_j), 4.6 ppm (d, 1H, H_k), 3.9 ppm (d, 1H, H_l), 2.7 ppm (s, 3H, H_m), 1.4−1.6 ppm (m, 54H, H_n). MALDI-TOF calculated for $C_{139}H_{86}N_8Zn$ = 1930.63 [M^+], 1902.62 [M − 28], 1182.62 [M − 748] (loss of C_{60} + N_2). Found: 1902.7 [M − 28], 1182.2 [M − 748].

m4p-ZnP−Triazole−C_{60} (**18**) was obtained in 31% yield by method 1 and 65% yield by method 2. ^{1}H NMR (400 MHz, $CDCl_3$): δ = 8.9−9.0 ppm (m, 9H, βH, triazole-H), 8.5 ppm (d, 1H, ArH), 8.3 ppm (d, 1H, ArH), 8.2 ppm (s, 1H, ArH), 8.1 ppm (s, 3H, ArH), 7.9−8.0 ppm (m, 4H, ArH), 7.75−7.77 ppm (m, 4H, ArH), 7.6 ppm (s, 1H, ArH), 7.4 ppm (s, 2H, ArH), 4.1 ppm (d, 1H, pyrrolidine-H), 3.8 ppm (s, 1H, pyrrolidine-H), 3.1 ppm (d, 1H, pyrrolidine-H), 2.5 ppm (s, 3H, *N*-methyl), 1.4−1.5 ppm (m, 54H, *tert*-BuH). MALDI-TOF calculated for $C_{139}H_{86}N_8Zn$ = 1930.63 [M^+], 1902.62 [M − 28], 1182.62 [M − 748] (loss of C_{60} + N_2). Found: 1903.3 [M − 28], 1182.3 [M − 748].

p4p-ZnP−Triazole−C_{60} (**19**) was obtained in ~30% yield by method 1. ^{1}H NMR (400 MHz, $CDCl_3$): δ = 8.9−9.0 ppm (m, 8H, βH), 8.8 ppm (s, 1H, Triazole-H), 8.4 ppm (d, 2H, ArH), 8.25 ppm (d, 2H, ArH), 8.16 ppm (d, 2H, ArH), 8.06 ppm (m, 6H, ArH), 7.8 ppm (m, 5H, ArH), 4.5 ppm (d, 1H, pyrrolidine-H), 4.4 ppm (s, 1H, pyrrolidine-H), 3.7 ppm (d, 1H, pyrrolidine-H), 2.7 ppm (s, 3H, *N*-methyl), 1.5 ppm (two singlets, 54H, *tert*-BuH). MALDI-TOF calculated for $C_{139}H_{86}N_8Zn$ = 1930.63 [M^+], 1902.62 [M − 28], 1182.62 [M − 748] (loss of C_{60} + N_2). Found: 1902.6 [M − 28], 1182.8 [M − 748]

p1p-ZnP−Triazole−C_{60} (**20**) was obtained in 34.5% yield by method 1. ^{1}H NMR (400 MHz, $CDCl_3$): 9.0 ppm (m, 8H, βH), 8.8 ppm (s, 1H, triazole-H), 8.4 ppm (d, 2H, ArH), 8.3 ppm (d, 2H, ArH), 8.2 ppm (d, 2H, ArH), 8.1 ppm (m, 6H, 3,5-di-*tert*-Bu-Ar-meta-H), 7.8 ppm (m, 5H, 3,5-di-*tert*-Bu-Ar-meta-H and ArH), 4.6 ppm (d, 1H, pyrrolidine-H), 4.5 ppm (s, 1H, pyrrolidine-H), 8.8 ppm (d, 1H, pyrrolidine-H), 2.8 ppm (s, 3H, *N*-methyl), 1.5 ppm (d, 54H, *tert*-BuH). MALDI-TOF mass calculated for $C_{139}H_{86}N_8Zn$ = 1930.63 [M+], 1902.63 [M − 28], 1182.63 [M − 28 − 720]. Found: 1902.37 [M − 28], 1183.58 [M − 28 − 720].

p1m-ZnP−Triazole−C_{60} (**21**) was prepared by method 2. ^{1}H NMR (400 MHz, $CDCl_3$): 9.0 ppm (m, 8H, βH), 8.8 ppm (s, 1H, triazole-H), 8.4 ppm (broad, 1H, ArH), 8.3 ppm (d, 2H, ArH), 8.2 ppm (d, 2H, ArH), 8.0 ppm (m, 6H, 3,5-di-*tert*-Bu-Ar-meta-H), 8.0 ppm (broad s, 1H, ArH), 7.7 ppm (m, 3H, 3,5-di-*tert*-Bu-Ar-para-H), 7.5 ppm (t, 1H, ArH), 4.8 ppm (s, 1H, pyrrolidine-H), 4.7 ppm (d, 1H, pyrrolidine-H), 4.0 ppm (d, 1H, pyrrolidine-H), 2.8 ppm (s, 3H, *N*-methyl), 1.5 ppm (d, 54H, *tert*-BuH). MALDI-TOF mass calculated for $C_{139}H_{86}N_8Zn$ = 1930.63 [M+], 1902.63 [M − 28], 1182.63 [M − 28 − 720]. Found: 1902.74 [M − 28], 1183.54 [M − 28 − 720].

p4m-ZnP−Triazole−C_{60} (**22**) was prepared by Method 1 from *p4m*-ZnP−Triazole−benzaldehyde (13 mg, 0.011 mmol), C_{60} (18.5 mg, 0.026 mmol), and sarcosine (8 mg, 0.09 mmol). The product was purified by column chromatography (silica gel,

dichloromethane). ^{1}H NMR (400 MHz, $CDCl_3$): δ = 8.9 ppm (m, 9H, βH, triazole-H), 8.3 ppm (d, 2H, ArH), 8.2 ppm (d, 2H, ArH), 8.0 ppm (m, 7H, ArH), 7.9 ppm (d, 1H, ArH), 7.8 ppm (m, 4H, ArH), 7.6 ppm (m, 1H, ArH), 4.7 ppm (m, 2H, pyrrolidine-H), 3.8 ppm (s, 1H, pyrrolidine-H), 2.8 ppm (s, 3H, *N*-methyl), 1.5 ppm (m, 54H, *tert*-BuH). MALDI-TOF calculated for $C_{139}H_{86}N_8Zn$ = 1930.63 [M+], 1902.62 [M − 28], 1182.62 [M − 748] (Loss of C_{60} + N_2). Found: 1184.9 [M − 748].

■ ASSOCIATED CONTENT

Supporting Information. IR, NMR, and mass spectra of all products and their precursors, calculated electron affinity data, calculated state energy values, differential pulse voltammetry data, and transient absorption spectra. This material is available free of charge via the Internet at http://pubs.acs.org.

■ AUTHOR INFORMATION

Corresponding Authors

david.schuster@nyu.edu; guldi@chemie.uni-erlangen.de

■ ACKNOWLEDGMENT

Support of the work at NYU by a grant from the National Science Foundation (CHE-0647334) is acknowledged with grateful appreciation. This investigation was conducted in part using an instrumental facility at NYU constructed with support from Research Facilities Improvement Grant Number C06 RR-16572-01 from the National Center for Research Resources, National Institutes of Health. O.L. and C.K.H. are grateful for support from the Dean's Undergraduate Research Fund at the NYU College of Arts and Science. We also thank Nathan Psota for technical assistance in the synthesis. Support is also gratefully acknowledged through a Senior Mentor Grant to DIS from the Camille and Henry Dreyfus Foundation. L.E. and A.O. gratefully acknowledge generous support from the US NSF, grant DMR-0809129. L.E. also thanks the Robert A. Welch Foundation for an endowed chair, grant # AH-0033. G. M. thanks the von Humboldt Foundation for a postdoctoral fellowship and Dr. Bruno Grimm for assistance with the steady-state spectroscopic measurements. D.M.G. thanks German Science Foundation (Cluster of Excellence − EAM-SFB-583) for support.

■ DEDICATION

Dedicated to Professor Harry B. Gray of the California Institute of Technology on the occasion of his 75th birthday.

■ REFERENCES

(1) (a) Cannon, R. D. *Electron Transfer Reactions*; Butterworths: London, U.K., 1980. (b) Eberson, L. *Electron Transfer Reactions in Organic Chemistry*; Springer: New York, 1987.

(2) Gust, D.; Moore, T. A.; Moore, A. L. *Acc. Chem. Res.* **2001**, *34*, 40.

(3) Imahori, H. *Bull. Chem. Soc. Jpn.* **2007**, *80*, 621.

(4) Kira, A.; Umeyama, T.; Matano, Y.; Yoshida, K.; Isoda, S.; Park, J. K.; Kim, D.; Imahori, H. *J. Am. Chem. Soc.* **2009**, *131*, 3198.

(5) Liddell, P. A.; Kuciauskas, D.; Sumida, J. P.; Nash, B.; Nguyen, D.; Moore, A. L.; Moore, T. A.; Gust, D. *J. Am. Chem. Soc.* **1997**, *119*, 1400.

(6) Kuciauskas, D.; Liddell, P. A.; Lin, S.; Johnson, T. E.; Weghorn, S. J.; Lindsey, J. S.; Moore, A. L.; Moore, T. A.; Gust, D. *J. Am. Chem. Soc.* **1999**, *121*, 8604.

(7) (a) Marcus, R. A. *J. Chem. Phys.* **1956**, *24*, 966. (b) Marcus, R. A. *J. Chem. Phys.* **1956**, *24*, 979. (c) Marcus, R. A. *J. Chem. Phys.* **1957**, *26*, 867. (d) Marcus, R. A. *J. Chem. Phys.* **1957**, *26*, 872. (e) Marcus, R. A. *Can. J. Chem.* **1959**, *37*, 155. (f) Guldi, D. M.; Fukuzumi, S. In *Fullerenes: From Synthesis to Optoelectronic Properties*; Guldi, D. M., Martin, N., Ed.; Kluwer Academic Publishers: Dordrecht, 2002; pp 237−265.

(8) (a) Guldi, D. M. *Chem. Soc. Rev.* **2002**, *31*, 22. (b) Drain, C. M.; Varotto, A.; Radivojevic, I. *Chem. Rev.* **2009**, *109*, 1630. (c) Holten, D.; Bocian, D. F.; Lindsey, J. S. *Acc. Chem. Res.* **2002**, *35*, 57.

(9) (a) Imahori, H.; Sakata, Y. *Adv. Mater.* **1997**, *9*, 537. (b) Echegoyen, L.; Echegoyen, L. E. *Acc. Chem. Res.* **1998**, *31*, 593. (c) Guldi, D. M. *Chem. Commun.* **2000**, *5*, 321. (d) Prato, M.; Guldi, D. M. *Acc. Chem. Res.* **2000**, *33*, 695. (e) Echegoyen, L.; Diederich, F.; Echegoyen, L. E. In *Fullerenes: Chemistry, Physics, and Technology*; Kadish, K. M., Ruoff, R. S., Ed.; Wiley-Interscience: New York, 2000; pp 1−53.

(10) (a) Bracher, P. J.; Schuster, D. I. In *Fullerenes: From Synthesis to Optoelectronic Properties*; Guldi, D. M., Martin, N., Ed.; Kluwer Academic Publishers: Dordrecht, 2002; pp 163−212. (b) Ikemoto, J.; Takimiya, K.; Aso, Y.; Otsubo, T.; Fujitsuka, M.; Ito, O. *Org. Lett.* **2002**, *4*, 309. (c) Vail, S. A.; Krawczuk, P. J.; Guldi, D. M.; Palkar, A.; Echegoyen, L.; Tome, J. P. C.; Fazio, M. A.; Schuster, D. I. *Chem.—Eur. J.* **2005**, *11*, 3375. (d) MacMahon, S.; Fong, R., II; Baran, P. S.; Safonov, I.; Wilson, S. R.; Schuster, D. I. *J. Org. Chem.* **2001**, *66*, 5449. (e) Ito, O. In *Handbook of Carbon Nano Materials. Volume 2. Electron Transfer and Applications*; D'Souza, F., Kadish, K. M., Ed.; World Scientific: Singapore, 2011; pp 441−477.

(11) (a) Rodriguez-Morgade, M. S.; Plonska-Brzezinska, M. E.; Athans, A. J.; Carbonell, E.; de Miguel, G.; Guldi, D. M.; Echegoyen, L.; Torres, T. *J. Am. Chem. Soc.* **2009**, *131*, 10484. (b) Imahori, H.; Fukuzumi, S. *Adv. Funct. Mater.* **2004**, *14*, 525. (c) O'Regan, B. C.; Lopez-Duarte, I.; Martinez-Diaz, M. V.; Forneli, A.; Albero, J.; Morandeira, A.; Palomares, E.; Torres, T.; Durrant, J. R. *J. Am. Chem. Soc.* **2008**, *130*, 2906.

(12) (a) Megiatto, J. D.; Schuster, D. I. *J. Am. Chem. Soc.* **2008**, *130*, 12872. (b) Megiatto, J. D.; Schuster, D. I. *Chem.—Eur. J.* **2009**, *15*, 5444. (c) Megiatto, J. D.; Spencer, R.; Schuster, D. I *Org. Lett.* **2009**, *11*, 4152. (d) Megiatto, J. D., Jr.; Schuster, D. I. In *Handbook of Carbon Nano Materials. Volume 1. Synthesis and Supramolecular Systems*; D'Souza, F., Kadish, K. M., Ed.; World Scientific: Singapore, 2011; pp 207−244. (e) Takata, T.; Ito, O. In *Handbook of Carbon Nano Materials. Volume 2. Electron Transfer and Applications*; D'Souza, F., Kadish, K. M., Ed.; World Scientific: Singapore, 2011; pp 479−517.

(13) (a) Collin, J.-P.; Harriman, A.; Heitz, V.; Odobel, F.; Sauvage, J.-P. *J. Am. Chem. Soc.* **1994**, *116*, 5679. (b) Schuster, D. I.; Cheng, P.; Wilson, S. R.; Prokhorenko, V.; Katterle, M.; Holzwarth, A. R.; Braslavsky, S. E.; Klihm, G.; Williams, R. M.; Luo, C. *J. Am. Chem. Soc.* **1999**, *121*, 11599. (c) Luo, C.; Guldi, D. M.; Imahori, H.; Tamaki, K.; Sakata, Y. *J. Am. Chem. Soc.* **2000**, *122*, 6535. (d) Schuster, D. I.; Cheng, P.; Jarowski, P. D.; Guldi, D. M.; Luo, C.; Echegoyen, L.; Pyo, S.; Holzwarth, A. R.; Braslavsky, S. E.; Williams, R. M.; Klihm, G. *J. Am. Chem. Soc.* **2004**, *126*, 7257.

(14) (a) Finn, M. G.; Fokin, V. V. *Chem. Soc. Rev.* **2010**, *39*, 1231. (b) Moses, J. E.; Moorhouse, A. E. *Chem. Soc. Rev.* **2007**, *36*, 1249.

(15) (a) Huisgen, R. *Pure Appl. Chem.* **1989**, *61*, 613. (b) Rostovtsev, V. V.; Green, L. G.; Fokin, V. V.; Sharpless, B. K. *Angew. Chem., Int. Ed. Engl.* **2002**, *41*, 2596. (c) Meldal, M.; Tornøe, C. W. *Chem. Rev.* **2008**, *108*, 2952–3015. (d) Huisgen, R.; Szeimies, G.; Moebius, L. *Chem. Ber.* **1967**, *100*, 2494. (e) Tornoe, C. W.; Christensen, C.; Meldal, M. *J. Org. Chem.* **2002**, *67*, 3057.

(16) (a) Hein, J. E.; Fokin, V. V. *Chem. Soc. Rev.* **2010**, *39*, 1302. (b) El-Sagheerab, A. H.; Brown, T. *Chem. Soc. Rev.* **2010**, *39*, 1388. (c) Jewetta, J. C.; Bertozzi, C. R. *Chem. Soc. Rev.* **2010**, *39*, 1272.

(17) (a) Gierlich, J.; Burley, G. A.; Gramlich, P. M. E.; Hammond, D. M.; Carell, T. J. *Org. Lett.* **2006**, *8*, 3639. (b) Chan, T. R.; Hilgraf, R.; Sharpless, K. B.; Fokin, V. V. *Org. Lett.* **2004**, *6*, 2853. (c) Franke, R.; Doll, C.; Eichler, J. *Tetrahedron Lett.* **2005**, *46*, 4479. (d) Jang, H.; Fafarman, A.; Holub., J. M.; Kirshenbaum, K. *Org. Lett.* **2005**, *7*, 1951. (e) Holub, J. M.; Jang, H.; Kirshenbaum, K. *Org. Biomol. Chem.* **2006**,

4, 1497. (f) Sun, X.-L.; Stabler, C. L.; Cazalis, C. S.; Chaikof, E. L. *Bioconjugate Chem.* **2006**, *17*, 52. (g) Nierengarten, J.-F.; Iehl, J.; Oerthel, V.; Holler, M.; Illescas, B. M.; Muñoz, A.; Martín, N.; Rojo, J.; Sánchez-Navarro, M.; Cecioni, S.; Vidal, S.; Buffet, K.; Durka, M.; Vincent, S. P. *Chem. Commun.* **2010**, *46*, 3860. (h) Sánchez-Navarro, M.; Muñoz, A.; Illescas, B. M.; Rojo, J.; Martín, N. *Chem.—Eur. J.* **2011**, *17*, 766.

(18) (a) Ladmiral, V.; Mantovani, G.; Clarkson, G. J.; Cauet, S.; Irwin, J. L.; Haddleton, D. M. *J. Am. Chem. Soc.* **2006**, *128*, 4823. (b) Diaz, D. D.; Punna, S.; Holzer, P.; McPherson, A. K.; Sharpless, K. B.; Fokin, V. V.; Finn, M. G. *J. Polym. Sci., Part A: Polym. Chem.* **2004**, *42*, 4392. (c) Ryu, E.-H.; Zhao, Y. *Org. Lett.* **2005**, *7*, 1035.

(19) (a) Lee, L. V.; Mitchell, M. L.; Huang, S.-J.; Fokin, V. V.; Sharpless, K. B.; Wong, C.-H. *J. Am. Chem. Soc.* **2003**, *125*, 9588. (b) Moorhouse, A. D.; Santos, A. M.; Gunaratnam, M.; Moore, M.; Neidle, S.; Moses, J. E. *J. Am. Chem. Soc.* **2006**, *128*, 15972. (c) Lewis, W. G.; Green, L. G.; Grynszpan, F.; Radic, Z.; Carlier, P. R.; Taylor, P.; Finn, M. G.; Sharpless, K. B. *Angew. Chem., Int. Ed.* **2002**, *41*, 1053. (d) Manetsch, R.; Krasinski, A.; Radic, Z.; Raushel, J.; Taylor, P.; Sharpless, K. B.; Kolb, H. C. *J. Am. Chem. Soc.* **2004**, *126*, 12809.

(20) Wu, P.; Malkoch, M.; Hunt, J. N.; Vestberg, R.; Kaltgrad, E.; Finn, M. G.; Fokin, V. V.; Sharpless, K. B.; Hawker, C. J. *Chem. Commun.* **2005**, 5775.

(21) Li, H.; Cheng, F.; Duft, A. M.; Adronov, A. *J. Am. Chem. Soc.* **2005**, *127*, 14518.

(22) Jarowski, P. D.; Wu, Y.—L.; Schweizer, B.; Diederich, F. *Org. Lett.* **2008**, *10*, 3347.

(23) Parent, M.; Mongin, O.; Kamada, K.; Katan, C.; Blanchard-Desce, M. *Chem. Commun.* **2005**, 2029.

(24) (a) Tkachenko, N. V.; Lemmetyinen, H.; Sonoda, J.; Ohkubo, K.; Sato, T.; Imahori, H.; Fukuzumi, S. *J. Phys. Chem. A* **2003**, *107*, 8834. (b) González-Rodríguez, D.; Torres, T.; Herranz, M. A.; Echegoyen, L.; Carbonell, E.; Guldi, D. M. *Chem.—Eur. J.* **2008**, *14*, 7670.

(25) (a) Appakkuttan, P.; Dehaen, W.; Fokin, V. V.; Van der Eycken, E. *Org. Lett.* **2004**, *6*, 4223. (b) Perez-Balderas, F.; Ortega-Munoz, M.; Morales-Sanfrutos, J.; Hernandex-Mateo, F.; Calvo-Flores, F. G.; Calvo-Asin, J. A.; Isac-Carcia, J.; Santoyo-Gonzalez, F. *Org. Lett.* **2003**, *5*, 1951. (c) Katritzky, A. R.; Singh, S. K. *J. Org. Chem.* **2002**, *67*, 9077.

(26) (a) Maggini, M.; Scorrano, G.; Prato, M. *J. Am. Chem. Soc.* **1993**, *115*, 9798. (b) Prato, M.; Maggini, M. *Acc. Chem. Res.* **1998**, *31*, 519.

(27) Lindsey, J. S.; Schreiman, I. C.; Hsu, H. C.; Kearney, P. C.; Marguerettaz, A. M. *J. Org. Chem.* **1987**, *52*, 827.

(28) Geier, G. R., III; Littler, B. J.; Lindsey, J. S. *J. Chem. Soc., Perkin Trans. 2* **2001**, 701.

(29) Chan, T. R.; Hilgraf, R.; Sharpless, K. B.; Fokin, V. V. *Org. Lett.* **2004**, *6*, 2853.

(30) Séverac, M.; Pleux, L. L.; Scarpaci, A.; Blart, E.; Odobel, F. *Tetrahedron Lett.* **2007**, *48*, 6518.

(31) Lindsey, J. S.; Brown, P. A.; Siesel, D. A. *Tetrahedron* **1989**, *45*, 4845.

(32) Imahori, H.; Hagiwara, K.; Aoki, M.; Akiyama, T.; Taniguchi, S.; Okada, T.; Shirakawa, M.; Sakata, Y. *J. Am. Chem. Soc.* **1996**, *118*, 11771.

(33) Wautelet, P.; LeMoigne, J.; Videva, V.; Turek, P. *J. Org. Chem.* **2003**, *68*, 8025.

(34) Eicher, T.; Hauptmann, S.; Speicher, A. In *The Chemistry of Heterocycles: Structure, Reactions, Synthesis, and Applications*, 2nd ed.; Wiley-VHC: New York, 2003; p 203.

(35) (a) Stewart, J. J. P. *J. Comput. Chem.* **1989**, *10*, 209. (b) Stewart, J. J. P *J. Comput. Chem.* **1989**, *10*, 221.

(36) Dewar, M. J. S.; Zoebisch, E. G.; Healy, E. F.; Stewart, J. J. P. *J. Am. Chem. Soc.* **1985**, *107*, 3902.

(37) (a) Zhao, Y.; Truhlar, D. G. *Theor. Chem. Acc.* **2008**, *120*, 215. (b) Zhao, Y.; Truhlar, D. G. *Acc. Chem. Res.* **2008**, *41*, 157.

(38) (a) Petersson, A.; Bennett, A.; Tensfeldt, T. G.; Al-Laham, M. A.; Shirley, W. A.; Mantzaris, J. *J. Chem. Phys.* **1988**, *89*, 2193. (b) Petersson, G. A.; Tensfeldt, T. G.; Montgomery, J. A., Jr. *J. Chem. Phys.* **1991**, *94*, 6091.

(39) Dunning, T. H., Jr.; Hay, P. J. In *Modern Theoretical Chemistry*; Schaefer, H. F., III, Ed.; New York: Plenum, 1976; Vol. 3, pp 1—28.

(40) Jarowski, P. D.; Wu, Y.-L.; Schweizer, B.; Diederich, F. *Org. Lett.* **2008**, *10*, 3347.

(41) Bard, A. J. Faulkner, L. R. *Electrochemical Methods: Fundamentals and Applications*, 2nd ed.; Wiley: New York, 2001.

(42) Electrochemical studies on **21** and **22** were not carried out, but there is no reason to expect major differences from what was observed with **17**—**20**.

(43) (a) Tat, F. T.; Zhou, Z.; MacMahon, S. A.; Song, F.; Rheingold, A. L.; Echegoyen, L.; Schuster, D. I.; Wilson, S. R. *J. Org. Chem.* **2004**, *69*, 4602. (b) Schuster, D. I.; Li, K.; Guldi, D. M.; Palkar, A.; Echegoyen, L.; Stanisky, C.; Cross, R. J.; Niemi, M.; Tkachenko, N. V.; Lemmetyinen, H. *J. Am. Chem. Soc.* **2007**, *129*, 15973.

(44) Imahori, H.; Tkachenko, N. V.; Vehmanen, V.; Tamaki, K.; Lemmetyinen, H.; Sakata, Y.; Fukuzumi, S. *J. Phys. Chem. A* **2001**, *105*, 1750.

(45) (a) Enescu, M.; Steenkeste, K.; Tfibel, F.; Fontaine-Aupart, M.-P. *Phys. Chem. Chem. Phys.* **2002**, *4*, 6092. (b) Baskin, J. S.; Yu, H.-Z.; Zewail, A. H. *J. Phys. Chem. A* **2002**, *106*, 9837.

(46) Luo, C.; Guldi, D. M.; Imahori, H.; Tamaki, K.; Sakata, Y. *J. Am. Chem. Soc.* **2000**, *122*, 6535.

(47) Imahori, H; Tamaki, H.; Guldi, D. M.; Luo, C.; Fujitsuka, M.; Ito, O.; Sakata, Y.; Fukuzumi, S. *J. Am. Chem. Soc.* **2001**, *123*, 2607.

(48) Guldi, D. M. *Chem. Commun.* **2000**, *5*, 321.

(49) In corresponding experiments in deoxygenated solutions, the triplet features of ZnP and/or C_{60} were clearly observed.

(50) Weller, A. *Z. Phys. Chem.* **1982**, *133*, 93.